POLITECNICO DI TORINO
Repository ISTITUZIONALE

Filtering acoustic from hydrodynamic velocity using modal decomposition methods on an acoustic liner under grazing turbulent flow

Original
Filtering acoustic from hydrodynamic velocity using modal decomposition methods on an acoustic liner under grazing turbulent flow / Scarano, F., Lyu, B., Paduano, A., Avallone, F.. - In: JOURNAL OF SOUND AND VIBRATION. - ISSN 0022-460X. - 625:(2026). [10.1016/j.jsv.2025.119568]

Availability:
This version is available at: 11583/3005457 since: 2025-11-26T13:19:58Z

Publisher:
Elsevier

Published
DOI:10.1016/j.jsv.2025.119568

Terms of use:

This article is made available under terms and conditions as specified in the corresponding bibliographic description in the repository

Publisher copyright

(Article begins on next page)

26 June 2026

Journal of Sound and Vibration 625 (2026) 119568

Contents lists available at ScienceDirect

Journal of Sound and Vibration

journal homepage: www.elsevier.com/locate/jsvi

Filtering acoustic from hydrodynamic velocity using modal decomposition methods on an acoustic liner under grazing turbulent flow

Francesco Scarano [a,*], Benshuai Lyu [b], Angelo Paduano [a], Francesco Avallone [a]

[a] Department of Mechanical and Aerospace Engineering (DIMEAS), Politecnico di Torino, Italy
[b] School of Mechanics and Engineering Science, Peking University, China

ARTICLE INFO

Keywords:
Modal decomposition
Spectral proper orthogonal decomposition
Canonical correlation decomposition
Acoustic liners
Acoustic induced velocity eduction
Separate acoustics from aerodynamics

ABSTRACT

The separation of acoustic-induced velocity from the turbulent velocity fluctuations is tackled on a numerical database representing a segment of an acoustic liner subjected to a grazing acoustic wave and turbulent flow. This scenario is meaningful due to the challenge of distinguishing sound-induced fluctuations from aerodynamic ones, and it has practical implications on the estimation of the liner's impedance and sound absorption properties. The separation is performed employing modal decomposition methods: proper orthogonal decomposition (POD), spectral proper orthogonal decomposition (SPOD), and canonical correlation decomposition (CCD). The acoustic-induced velocity is reconstructed by selecting a limited number of modes representative of the acoustic-induced flow. All the decomposition methods are influenced by the acoustic-to-hydrodynamic fluctuation ratio, i.e., the relative amplitude of the acoustic waves and turbulent fluctuations. The CCD and SPOD outperform POD when the acoustic amplitude is low compared to the flow turbulence intensity. The acoustic forcing frequency must be known a priori or easily identifiable in the spectrum for SPOD. CCD better captures non-linear effects, e.g., due to the vortex shedding at high sound pressure levels, which are associated with high-order modes.

1. Introduction

In the realm of computational aeroacoustics or when performing time-resolved measurements of a turbulent field, the instantaneous pressure and velocity fields encompass both coherent (i.e., acoustics) and non-coherent (i.e., aerodynamics) fluctuations [1]. In computational aeroacoustics, the instantaneous velocity and pressure fields are usually obtained by solving compressible flow equations [2]; therefore, the two components are intrinsically coupled. However, in several domains, studying the two distinct fields and how they interact is of pivotal interest. As stated by Arndt et al. [3], separating the two components requires sophisticated filtering procedures.

In many applications of interest, the hydrodynamic or aerodynamic component is only marginally influenced by compressibility [4]. In contrast, the acoustic field, associated with sound waves that propagate at the speed of sound, is described by the linear wave equation. The acoustic component can be generated by either unsteady turbulent structures, such as in jet noise [1] or turbulent

* Corresponding author.
E-mail addresses: francesco.scarano@polito.it (F. Scarano), b.lyu@pku.edu.cn (B. Lyu), angelo.paduano@polito.it (A. Paduano), francesco.avallone@polito.it (F. Avallone).

https://doi.org/10.1016/j.jsv.2025.119568
Received 1 April 2025; Received in revised form 17 November 2025; Accepted 22 November 2025
Available online 25 November 2025
0022-460X/© 2025 The Author(s). Published by Elsevier Ltd. This is an open access article under the CC BY license (http://creativecommons.org/licenses/by/4.0/).

boundary layer trailing edge noise, or by an external source interacting with the turbulent field. In the first case, filtering the acoustic velocity allows gaining a better understanding of the sound generation and propagation mechanisms in the far field.

The latter scenario describes, for example, an acoustic wave that interacts with a turbulent flow, such as for acoustic liners installed on a nacelle of an engine [5]. The intricate physics behind the noise absorption mechanism of acoustic liners leads to a strong coupling between the acoustic-induced flow, which is generated by the external source and induced within the orifices of the liner face sheet, and the turbulent boundary layer. This interaction affects the noise-absorption properties of the liner by modifying its acoustic impedance [6]. To fully understand and correctly model how this happens, isolating the acoustic-induced flow field is essential [7]. In addition, the evaluation of the acoustic-induced velocity field can be used to compute the sound dissipation or generation by vortical structures [8–10]. The challenges in separating the acoustic from the hydrodynamic field and its repercussions for industrial scenarios make the acoustic liner case a valuable benchmark to test filtering techniques.

Several post-processing methods attempted to decompose the aerodynamic and the acoustic-induced components starting from velocity or pressure time series acquired from experiments or simulations. The most widely-used methods are frequency-wavenumber decomposition [11], Helmholtz decomposition [2,12], wavelet decomposition [13] and dynamic mode decomposition [14].

The frequency-wavenumber decomposition has been applied by Arguillat et al. [11] to separate the acoustic and the aerodynamic components from instantaneous pressure measurements beneath a turbulent channel flow in an anechoic wind tunnel. This technique imposes constraints on the spacing and distances between the reference probes; therefore, it is more suited for experimental investigation of non-complex geometries [2]. Nonetheless, it has recently been applied by Vincent and Bogey [15] to isolate aerodynamic fluctuations in a numerical dataset.

Helmholtz decomposition [2,12] aims at separating irrotational and solenoidal fields (incompressible if for velocity). The velocity field is decomposed into a rotational (vortical) and an irrotational part; it is assumed that the acoustic contribution is irrotational while the aerodynamic contribution is incompressible. The acoustic contribution is obtained by solving an inhomogeneous Poisson equation in the entire domain and for each snapshot. This is computationally expensive in the case of complex geometries. The method is intrinsically valid for a three-dimensional field while posing problems at the boundaries and corners of a solid domain, where the Poisson equation must be locally valid.

Alternative postprocessing strategies have also been developed based on acoustic wave equations. A well-known example is the Acoustic Perturbation Equations (APE) by Ewert and Schröder [16], which enables the separation of hydrodynamic and acoustic fluctuations by introducing excitation source terms into the linearized perturbation equations. This formulation is generally applicable in linear regimes. More recently, Schoder et al. [17] proposed the Aeroacoustic Wave Equation based on Pierce's Operator (AWE-PO), which embeds convective effects directly into the wave operator with the aim to predict the flow-induced sound field.

A wavelet-based procedure to separate aerodynamic from acoustic instantaneous pressure in turbulent jets was first developed by Grizzi and Camussi [18] and then improved by Mancinelli et al. [1]. The method assumes that the hydrodynamic pressure, caused by the turbulent structures, is intermittent. This contribution can then be better decomposed into a wavelet basis rather than a Fourier basis. The hydrodynamic component can be isolated from the acoustic component by selecting the wavelet coefficients that exceed a threshold to be found iteratively by correlating the signal of two microphones in the near field.

The current study focuses on modal decomposition methods, which enable the decomposition of an instantaneous velocity or pressure field into a defined set of modes. These modes are typically ranked according to their dynamics, energy, or correlation strength, and are associated with the so-called coherent structures. By utilizing only a limited number of modes, the most significant features of the velocity or pressure field can be captured, and a reduced-order or low-rank model can be created. The latter can be used to reconstruct the velocity or the pressure field, thus using the modal decomposition method as a filtering technique.

The dynamic mode decomposition (DMD) is based on global stability analysis and allows for obtaining dynamic information from experimental or numerical unsteady data. The technique has been used to extract self-sustained oscillations in a flow over a square cavity [14]. The recent study by Brunner et al. [19] has employed Dynamic Mode Decomposition (DMD) to analyse the acoustic modes and feedback mechanisms in deep cavities with overhanging lips, providing insights into the noise generation processes.

Proper orthogonal decomposition (POD) [20,21] decomposes a turbulent field into modes, with each mode representing a specific portion of the total turbulent kinetic energy. POD can be used to investigate physical phenomena for which ranking the coherent structures in terms of turbulent kinetic energy is sufficient to separate the aerodynamic from the acoustic field. Mancinelli et al. [13] applied POD in combination with frequency-wavenumber decomposition on streamwise microphone signals. Using this approach, they described the coherent streamwise evolution of a compressible jet and gave a hydrodynamic/acoustic interpretation to the POD modes thanks to the frequency-wavenumber decomposition.

Spectral proper orthogonal decomposition (SPOD) [22,23] has the advantage of extracting modes coherent in space and frequency. For this reason, it can be used to identify and filter out the energetically relevant structures at a known frequency.

Unlike POD, the recently developed canonical correlation decomposition (CCD) [24,25] seeks to extract coherent structures ranked by their corresponding correlation strength with a reference signal. This could suit our purposes of extracting acoustically driven flow structures. By choosing the acoustic forcing as the observable, the coherent flow structures correlated with it can be identified, thus revealing the acoustic-induced velocity. Further details on POD, CCD, and SPOD are provided below.

In this study, we investigate the possibility of separating the acoustic and aerodynamic velocity components by identifying the corresponding coherent modes in the flow field. The use of modal decomposition as a filtering technique to extract the acoustic-induced velocity has not been extensively examined in the existing literature. The selected case study is the flow over an acoustic liner. In addition, we will compare the results with the triple decomposition. This technique is widely used in acoustic liner studies [5,6,26] for separating acoustic-induced velocity from aerodynamic fluctuations when the acoustic forcing frequency is known.

However, we will show that triple decomposition performances deteriorate in non-linear or highly turbulent regimes. Therefore, in the present study it is employed solely as a reference for comparison with the modal decomposition methods.

The paper is structured as follows. In Section 2, the modal decomposition methods are detailed. The numerical setup, details on the flow and acoustic physics of acoustic liners, and the motivation behind the setup are described in Section 3. The results of the modal decomposition are shown in Section 4. In Section 5, the acoustic-induced velocity is obtained through a low-order model reconstruction; the contours of the reconstructed velocity and the velocity profiles at various phases, i.e., from the inflow to the outflow, are shown. The main conclusions and a summary of the results are presented in Section 6.

2. Decomposition methods

2.1. Proper orthogonal decomposition (POD)

Lumley [27] introduced POD to extract coherent flow structures from a turbulent velocity field. Each POD mode captures a certain portion of the total turbulent kinetic energy in the flow.

A given instantaneous velocity field can be written as $\boldsymbol{u'}(\boldsymbol{x},t) = \overline{\boldsymbol{u}}(\boldsymbol{x}) + \boldsymbol{u}(\boldsymbol{x},t)$, where $\overline{\boldsymbol{u}}$ is the time-averaged velocity and $\boldsymbol{u}$ is the instantaneous velocity fluctuation. Then, the fluctuating field can be decomposed as:

$$\boldsymbol{u}(\boldsymbol{x},t) = \sum_{k=1}^{\infty} c_k(t)\boldsymbol{\Phi}_k(\boldsymbol{x}), \tag{1}$$

where $\boldsymbol{\Phi}_k(\boldsymbol{x})$ represents the POD modes, which are functions only of space and are mutually orthogonal. The temporal evolution of each mode is described by the coefficient $c_k(t)$. This decomposition maximizes the turbulent kinetic energy of the resulting POD modes.

Suppose a high percentage of the turbulent kinetic energy is retained in one or a few modes k_n. In that case, the flow can be seen as coherent, and it is possible to create a reduced-order model, also called a low-rank model, of the velocity field using a limited number of POD modes. This approach will be used in Section 5 to reconstruct the acoustic-induced velocity field.

The procedure to apply POD is summarized as follows. Suppose that the flow is sampled at times t_1, t_2, t_3 $\ldots t_N$. This yields a collection of snapshots $\boldsymbol{u}_1$, $\boldsymbol{u}_2$, $\boldsymbol{u}_3 \ldots \boldsymbol{u}_N$, where N is an integer. One can write the collections of flow snapshots $\boldsymbol{u}_i$ in a compact matrix form as

$$\boldsymbol{U} = \quad [\boldsymbol{u}_1, \boldsymbol{u}_2, \boldsymbol{u}_3 \ldots \boldsymbol{u}_N], \tag{2}$$

Among the several methods to perform POD and extract the modes, the simplest procedure makes use of the singular value decomposition on the snapshot matrix $\boldsymbol{U}^T/\sqrt{N-1} = \boldsymbol{L}\boldsymbol{\Sigma}\boldsymbol{R}^T$. Each matrix column $\boldsymbol{R}$ represents a POD mode, while its energy fraction is given by its corresponding singular value's square embedded in the diagonal matrix $\boldsymbol{\Sigma}$.

A comprehensive review of the POD can be found in Berkooz et al. [20] while the reader should refer to Weiss [21] for a more practical view of the technique applied to experimental data.

2.2. Canonical correlation decomposition (CCD)

CCD aims to decompose a flow of a complex nature based on a correlation ranking [24]. The resulting modes are mutually orthogonal and form a complete set. They are ranked according to their correlation strength with a given observable. Therefore, if the observable is independent of some flow structures, CCD would effectively exclude them from the resulting modes, even though they may be highly energetic. This targets the observable exclusively and is therefore suitable for identifying the source and descent structures of the observable.

The essential procedure to conduct CCD is summarized as follows. Suppose that the flow is sampled at time t_1, t_2, t_3 $\ldots t_N$ to yield a collection of snapshots $\boldsymbol{u}_1$, $\boldsymbol{u}_2$, $\boldsymbol{u}_3 \ldots \boldsymbol{u}_N$, where N is an integer. Assume that the observable p is sampled simultaneously with the flow. In particular, the sequence p_{11}, p_{12}, p_{13}, $\ldots p_{1Q}$ (Q is an integer) is sampled at times $t_1+\tau_1$, $t_1+\tau_2$, $t_1+\tau_3$ $\ldots t_1+\tau_Q$, respectively, where τ_j ($j = 1, 2, 3, .Q$) represents the time delay with respect to the sampling time t_1. This sequence is then written as a column vector $\boldsymbol{p}_1$. Similarly, $\boldsymbol{p}_2$, $\boldsymbol{p}_3 \ldots \boldsymbol{p}_N$ can be constructed with respect to time t_2, t_3 and t_N. One can write the collections of flow snapshots $\boldsymbol{u}_i$ and observables $\boldsymbol{p}_i$ in compact matrix forms as

$$\begin{aligned} \boldsymbol{U} &= \quad [\boldsymbol{u}_1, \boldsymbol{u}_2, \boldsymbol{u}_3 \ldots \boldsymbol{u}_N], \\ \boldsymbol{P} &= \quad [\boldsymbol{p}_1, \boldsymbol{p}_2, \boldsymbol{p}_3 \ldots \boldsymbol{p}_N]. \end{aligned} \tag{3}$$

Upon defining the correlation matrix $\boldsymbol{A} = 1/(\sqrt{Q}N)\boldsymbol{P}\boldsymbol{U}^{\dagger}$, where $\dagger$ denotes Hermitian conjugate, one can obtain the CCD modes by performing the singular value decomposition of $\boldsymbol{A} = \boldsymbol{R}\boldsymbol{\Sigma}\boldsymbol{V}^{\dagger}$. Each column of $\boldsymbol{V}$ represents a CCD mode, while its correlation strength with the observable is given by its corresponding singular value's square embedded in the diagonal matrix $\boldsymbol{\Sigma}$.

In this paper, the upstream acoustic forcing pressure is the observable. The sampling frequency of the flow and the observable are the same. The total number of snapshots is $N - Q + 1$, where N is the total recorded snapshots of the flow described in detail in Section 3.3, and Q is taken as $N/4$. Considering the causal time delay between the forcing and the downstream structures, τ_1 is assumed to be a negative value of $-2Q/3f_s$, where f_s is the sampling frequency of the flow, further details are reported in the Appendix B.

2.3. Spectral proper orthogonal decomposition (SPOD)

SPOD is a technique that allows the extraction, from statistically stationary data, of an optimal orthogonal basis where a high fraction of the total energy is retained in a few modes that are coherent in time and space. As stated by Schmidt and Colonius [23], SPOD has the advantages of POD and DMD combined; it captures the temporal correlations within the resulting structures and the optimality inherent in POD.

The procedure to apply SPOD is summarized as follows. Suppose that the flow is sampled at time $t_1, t_2, t_3 \ldots t_N$ to yield the collection of all the snapshots $\boldsymbol{u}_1, \boldsymbol{u}_2, \boldsymbol{u}_3 \ldots \boldsymbol{u}_N$, where N is an integer. We can divide the series of the snapshots into a certain number of blocks, N_{blk}, and compute the discrete Fourier transform of each block using the Welch averaging method $\hat{\boldsymbol{u}}_1, \hat{\boldsymbol{u}}_2, \hat{\boldsymbol{u}}_3 \ldots \hat{\boldsymbol{u}}_{N_{blk}}$. Each block has a certain percentage of overlap with the next block. In analogy with POD, one can then write the collections of Fourier-transformed snapshots $\hat{\boldsymbol{u}}_i$ in compact matrix forms as:

$$\hat{\boldsymbol{U}}(f) = \quad [\hat{\boldsymbol{u}}_1, \hat{\boldsymbol{u}}_2, \hat{\boldsymbol{u}}_3 \ldots \hat{\boldsymbol{u}}_{N_{blk}}]. \tag{4}$$

This results in one complex matrix $\hat{\boldsymbol{U}}(f)$ for each of the frequencies obtained by the Fourier decomposition. The cross-spectral density matrix (CSD) of the samples is then computed at each frequency as

$$\boldsymbol{S} = 1/(N-1)\hat{\boldsymbol{U}}\hat{\boldsymbol{U}}^{\dagger} \tag{5}$$

where † is the Hermitian conjugate of the complex matrix. The SPOD modes are then obtained by computing the eigenvectors of the CSD at each frequency.

The Matlab routines by Towne et al. [22] are used as a framework to perform the decomposition and reconstruct the velocity field.

2.4. Acoustic-induced velocity estimation based on reduced order model

The acoustic-induced velocity field is obtained after the modal decompositions. The vertical velocity component is investigated because it is the one commonly adopted to describe the in-orifice flow field [6,26,28], thus allowing to compare the present results with the ones in the literature, at least in a qualitative way. The same decomposition-reconstruction procedure can be applied to the streamwise component or the pressure. A reduced order model is obtained for all the decomposition methods by selecting the desired number of modes, k_n, representing the acoustic-induced velocity field.

The modes for the reconstruction are selected based on their energy (POD) or correlation strength (CCD) and mode shape. An additional parameter for the selection is the spectral content of the coefficients associated with each mode. Its analysis can reveal that the mode is associated with a certain dominant frequency. A reduced-order model (ROM) is built based on the first three POD and CCD modes. From a practical standpoint, regarding the choice of the number of modes for the ROM, if the singular values' square of the POD, SPOD or CCD decay more than one or even two orders of magnitude, the reconstruction is usually good. In POD and SPOD, this suggests that the reconstruction captures most of the kinetic energy, while in CCD, this suggests that it captures most of the energy that is correlated with the observable. The procedure to obtain the reconstructed velocity field for the SPOD is slightly different. The ROM is obtained by considering the first two modes or only the first mode at two frequency bands, as illustrated later when describing the spectra. For this reason, a band-pass filter is applied to the SPOD coefficients. The frequency band for the filter needs to be selected before the reconstruction. In the current investigation, the frequency interval is centered at the source frequency (1.4 kHz) and its first harmonic (2.8 kHz), which are known a priori. The frequency bandwidth is a free parameter for the reconstruction. An analysis carried out, but not shown for conciseness, showed that selecting any bandwidth between 50 and 350 Hz does not affect the results.

The acoustic-induced velocity obtained from the ROM corresponds to the coherent contribution extracted through modal decomposition. It is important to emphasize that this coherent fraction cannot be directly equated with the irrotational component of the velocity field, as in a Helmholtz decomposition. Instead, the ROM represents the portion of the flow that most closely captures the coherent acoustic-induced velocity.

The reconstructed velocity fields from the three decomposition methods are compared with the triple decomposition. Note that the triple decomposition method is included here not as a benchmark or absolute reference, but as a simpler technique for separating acoustic-induced velocity from aerodynamic velocity in acoustic liner research [5,6,26]. For clarity the triple decomposition is summarized here: the time-series data are phase-locked with the incoming acoustic wave, effectively filtering out the uncorrelated velocity fluctuations associated with the turbulent grazing flow. This phase-locking process averages out turbulence-driven fluctuations, leaving the acoustic-related components intact. Next, the time average of the phase-locked flow field is computed, providing a steady-state representation of the flow. Finally, this time-averaged component is subtracted from the phase-locked measurements. The resulting data represent the acoustic-induced velocity, which can be interpreted as the flow variations induced by the periodic acoustic wave interacting with the orifice, and not by any steady flow associated with the grazing turbulent flow.

3. Numerical database and flow description

3.1. Methodology

This study uses the simulation database described in Paduano et al. [28]. Simulations were conducted with 3DS Simulia PowerFLOW (v6), a solver based on the lattice Boltzmann method (LBM). This approach solves the discretized Boltzmann equation in space

and time [29]:

$$\frac{\partial g}{\partial t} + \vec{\xi} \cdot \nabla g + F \cdot \nabla_{\xi} g = \Omega, \tag{6}$$

where $g(\vec{\xi}, \vec{x}, t)$ represents the probability distribution for a particle at position $[\vec{x}, \vec{x} + \Delta\vec{x}]$, with velocity $[\vec{\xi}, \vec{\xi} + \Delta\vec{\xi}]$, during time step $[t, t + \Delta t]$. The left-hand side accounts for particle transport and external forces, while the Bhatnagar-Gross-Krook (BGK) collision operator [30], on the right-hand side, models particle interactions. The latter is:

$$\Omega = -\frac{1}{\tau}(g - g^{eq}), \tag{7}$$

where τ is the relaxation time, and g^{eq} is the equilibrium distribution based on the Maxwell-Boltzmann distribution. The BGK formulation indicates that the local distribution function g relaxes to the equilibrium distribution g^{eq} over a characteristic time scale defined by τ.

The LBM is solved on a Cartesian lattice (voxels) where particles move in discrete directions with specific velocities and time steps. For the present study, the LBM solver employs a 3-dimensional lattice with 19 discrete velocity directions, commonly referred to as the D3Q19 model [31]. The present work adopts a very large eddy simulation (VLES) approach, which resolves large turbulence scales while modeling sub-grid scales through an effective relaxation time. This relaxation time combines the viscous relaxation time with an additional turbulent relaxation time. The turbulence model, based on the formulation of $k - \epsilon$ re-normalisation group (RNG) [32], defines the effective relaxation time:

$$\tau_{\text{eff}} = \tau + C_{\mu} \frac{k^2/\epsilon}{(1 + \eta^2)^{1/2}}, \tag{8}$$

where $C_{\mu} = 0.09$, and η combines local strain, vorticity, and helicity, reducing sub-grid scale viscosity in regions with large vortical structures. It should be pointed out that the usage of the $k - \epsilon$ RNG model under the LBM framework differs significantly from its application in Reynolds-Averaged Navier-Stokes (RANS) simulations. A pressure-gradient-based wall model is adopted to reduce the computational cost.

3.2. Numerical setup

The computational domain is described in detail in Paduano et al. [28]. The liner is positioned on the top wall of a rectangular duct, as illustrated in Fig. 1. It consists of eleven cavities with square cross-sections ($l = 12.14$ mm) and cavity depths ($D = 38.1$ mm). Each cavity contains eight orifices having a diameter equal to $d = 1.17$ mm with slightly rounded edges. The partition walls have a thickness of $w_p = 2.53$ mm, and the face sheet has a thickness of $\tau = 0.54$ mm. These dimensions result in an open area percentage (also called porosity) of 7.02 %. The resonant frequency of this liner in the absence of grazing flow is 1.4 kHz while it shifts to larger values in the presence of the flow.

The streamwise coordinate x is aligned with the flow direction, from left to right in the figures. The spanwise coordinate is z and the vertical coordinate is y. The origin of the vertical coordinate is on the side of the face sheet exposed to the flow. The y axis is positive entering the cavity.

Quasi-anechoic conditions were achieved at the duct termination by exponentially increasing the fluid viscosity in sponge regions by a factor of 100. All walls were treated as adiabatic, with a uniform flow imposed at the inlet and a pressure boundary condition applied at the outlet. Periodic boundary conditions were imposed along the lateral sides of the domain. A zig-zag trip was placed upstream of the liner at $x = -1600$ mm to trigger boundary layer transition. The zig-zag trip has a height of 0.25 mm and a length of 2 mm. This was done in order to match the boundary layer profile in the experiments carried out by Bonomo et al. [33].

A variable resolution (VR) scheme was applied to discretize the domain. The resolution varies by a factor of two between adjacent VR regions. The grid is symmetric with respect to the channel centreline. A total of six VR regions were adopted, becoming coarser away from the liner. The finest grid resolution was used over the entire face sheet, the orifices, and the backing cavity. Inside the orifice, the minimum spacing of the grid was $\Delta z_{\text{min}} = \Delta y_{\text{min}} = \Delta x_{\text{min}} = 0.0234$ mm, resulting in an effective resolution of approximately 50 voxels/d. The mesh independent study is presented in [28].

The simulation approach is based on two steps: first, the spatially developing boundary layer is obtained. Then, after the transient, an instantaneous flow field was saved and modified by overlaying a plane acoustic wave with specified frequency and amplitude using the *OptydB* toolkit. This modified flow field served as the initial condition for the acoustic simulations. This two-step approach explicitly captures the interaction between acoustic waves and unsteady turbulence [5,34]. This is fundamentally different from methodologies based on the linearized Navier–Stokes equations, in which acoustic perturbations are superimposed onto a mean flow, typically obtained from Reynolds-averaged Navier–Stokes (RANS) computations, and the acoustic field is solved independently of the turbulent dynamics (RANS + computational aeroacoustics) [35]. Moreover, the methodology used in this work captures the inherently nonlinear response of the liner when exposed to a grazing acoustic wave at 145 dB, since the interaction between the unsteady turbulence and the imposed acoustic field is directly resolved rather than assumed linear a priori. The main drawback of this approach is the requirement for the computational domain to be sufficiently long to accommodate at least ten acoustic wavelengths of the lowest frequency of interest. However, this method significantly reduces computational costs when evaluating multiple configurations, making it an efficient choice for parametric studies.

The dataset on which the decomposition is performed is a 2D field cropped in the vicinity of one of the orifices as depicted in Fig 1(b) and (c). The first orifice of the most upstream cavity is selected for the analysis, as it is exposed to the strongest acoustic

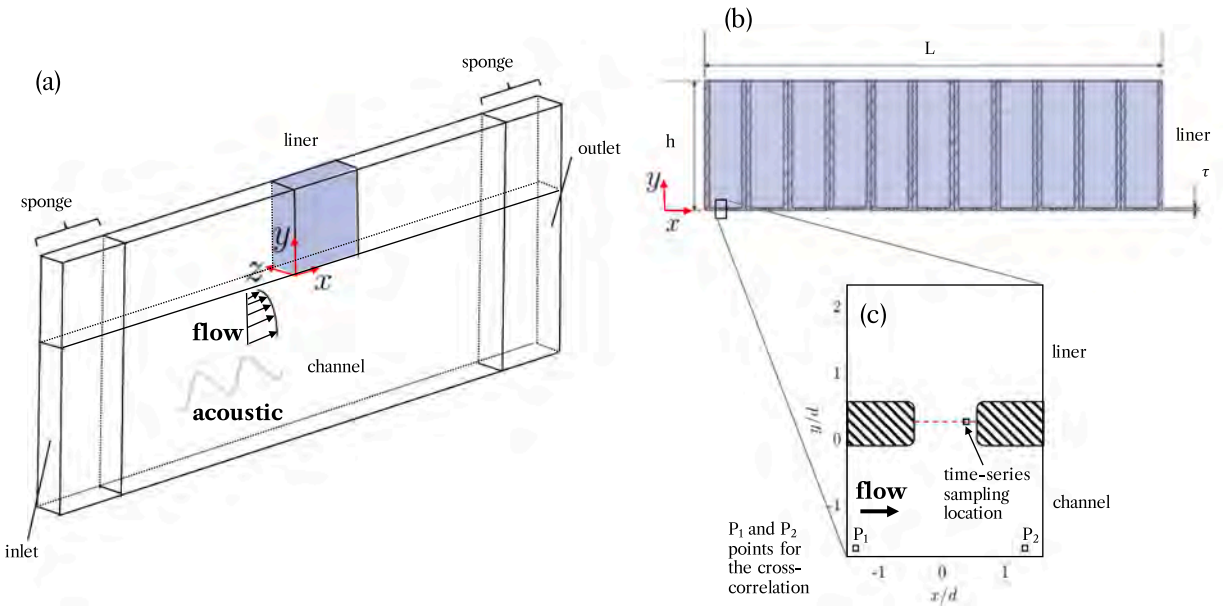

Fig. 1. Sketch of the numerical setup (a) 3D geometry, (b) 2D cross-plane of the acoustic liner, (c) orifice and domain analyzed.

Table 1
List of the simulations analyzed in this work.

Mach number	SPL (dB)	Frequency (kHz)
0	130	1.4
0	145	1.4
0.32	130	1.4
0.32	145	1.4

forcing without attenuation from upstream cavities, and the grazing flow is unaffected by any preceding cavities. Fig. 1(c) details the sub-domain investigated in this study. Furthermore, the figure shows the point at the middle of the face sheet thickness where the time series presented in the paper are sampled, and the points P_1 and P_2 used in Section 5.4 to compute the convective velocity from the filtered data. Furthermore, the dashed red line in the figure represents the location where the velocity profiles presented in Section 5.3 are sampled.

The nomenclature for the velocity components is the following: u', v', w' are the instantaneous velocity components, $\overline{u}, \overline{v}, \overline{w}$ stand for the time-average values, and u, v, w are the fluctuating components according to the Reynolds decomposition.

3.3. Description of the numerical database

Four test cases are investigated. In the first two, the liner is grazed only by an acoustic plane wave, while in the other two, there is a plane acoustic wave and a grazing flow with a centreline Mach number of 0.32 and a bulk Mach number of 0.3. The flow and the acoustic wave propagate from left to right in the domain. Two different acoustic sound pressure levels (SPL) are tested: 130 and 145 dB. The reported SPL is evaluated at the channel centreline upstream of the cavity. The source frequency is set equal to 1.4 kHz, which is the resonant frequency of the liner in the absence of flow. Only one frequency is selected for the sake of conciseness. The decomposition methods are applicable to other single-tone forcing frequencies; however, moving away from the resonant frequency reduces the amplitude of the acoustic-induced velocity, effectively lowering the acoustic-to-hydrodynamic fluctuation ratio (AHFR) at a given SPL. For this reason using frequencies far from resonance produces similar trends to those reported here, with the AHFR decrease being equivalent to reducing the SPL at the resonant frequency.

The cases tested are summarized in the Table 1. Each dataset consists of $N = 4740$ snapshots with a sampling frequency of 420 kHz, which corresponds to about 16 acoustic periods.

The two SPL values are selected because, conventionally, based on the literature, in the absence of flow, they correspond to the linear and non-linear operating regimes. When the incident acoustic amplitude is below 130 dB, the liner operates predominantly in the linear regime, where acoustic energy is dissipated through viscous effects along the internal walls of the orifices [36]. At higher SPLs, the dissipation mechanism is increasingly governed by the formation of turbulent jets and vortex shedding at the orifice openings [26,35]. For geometries similar to the one analysed here, Tam and Kurbatskii [36] reported that the onset of vortex formation, typical

of the non-linear regime, occurs above 140 dB, a result that is consistent with our preliminary studies on the acoustic dissipation [37]. Nevertheless, small non-linearities may still be present at 130 dB.

In both regimes, the acoustic plane wave induces periodic inflow and outflow motions through the liner orifice [6]. The cycle of an acoustic wave passage is defined as ϕ. During a cycle, the inflow phase ($\phi = \pi/2$) corresponds to the moment when there is the maximum injection of mass flow in the cavity through the orifice, while the outflow phase ($\phi = 3\pi/2$) represents the instance when there is the maximum ejection of mass flow.

In the case of the grazing flow, the non-linearity of the flow dominates. From a physical point of view, there is a reduction of the effective porosity of the liner because of the formation of a vortex on the upstream edge of the orifice. This results in the inflow and outflow velocity profiles localized in the downstream half of the orifice [6].

Fig. 2(a) shows a randomly chosen snapshot of the vertical velocity fluctuation for the case with $M = 0.32$ and SPL = 145 dB. The figure highlights that the turbulence interacts with the sound-induced flow. In Fig. 2(b), the time series of the static pressure is shown for the cases where there is only the flow, and also the acoustic waves with two SPLs. For SPL = 130 dB, there is not much difference between the cases with and without acoustic forcing. On the other hand, for the case at SPL = 145 dB, the acoustic excitation is easily detectable. This can be interpreted as a variation of the AHFR. The corresponding spectra are shown in Fig 2(c), where it is evident that the energy associated with the acoustic source frequency, i.e., 1.4 kHz, increases when the SPL increases. A second peak at 14 kHz can be identified for both SPLs. The 14 kHz tone is also present without the acoustic forcing because it is associated with a cavity depth mode. Further theoretical details about this cavity mode can be found in [38] with experimental evidence shown by Dacome et al. [39]. This additional high-frequency fluctuation, which accounts for a high energetic content, challenges the acoustic/aerodynamic decomposition as it will act as an additional sharp "disturbance" in the system.

The reconstructed acoustic velocity field is normalized by a theoretical reference velocity obtained from the lumped-element model of a Helmholtz resonator [40]. The amplitude of the theoretical acoustic velocity is expressed as

$$v^*_{ac} = \frac{p}{\rho\omega(\tau + 0.8d)} \frac{1}{\sqrt{\left[\left(\frac{\omega_H}{\omega}\right)^2 - 1\right]^2 + \left(\frac{\omega_H}{\omega Q}\right)^2}}, \tag{9}$$

where p is the amplitude of the pressure fluctuations in the orifice, ω and ω_H are the forcing and resonant frequency, Q is the quality factor (here set to the conventional value of 10), ρ is the density, and d and τ are the orifice diameter and thickness, respectively.

This formulation provides the maximum amplitude of the theoretical acoustic-induced velocity within the orifice during both the inflow (positive) and outflow (negative) phases. For instance, it yields values of 5.76 m/s at 130 dB and 25.96 m/s at 145 dB. Although the model was originally derived without grazing flow and for an acoustic wave normal to the orifice, it has been widely adopted in studies of acoustic liners under grazing acoustic waves and grazing flow [6].

Among possible choices for normalization (e.g., free-stream velocity, friction velocity, speed of sound), this theoretical acoustic velocity is the most suitable. It not only provides a physically consistent reference but also allows verifying the order of magnitude of the reconstructed velocity field. Specifically, in cases without grazing flow, the normalized acoustic velocity should be of order unity, whereas it should decrease below unity when grazing flow is present [26].

We remind here that the theoretical acoustic velocity, v^*_{ac}, is valid for a perfectly sharp orifice while in the current case the edges are slightly rounded to mimic an experimental campaign conducted by Bonomo et al. [33] used as reference. In addition, a theoretical response of the acoustic wave can only be obtained for an acoustic wave normal to the Helmholtz resonator, while in the current investigation the acoustic wave is grazing. This latter consideration in particular can explain small discrepancies between the reconstructed and the theoretical acoustic-induced velocity.

4. Modal decomposition results

In this section, the results of the application of each modal decomposition technique are reported. As the main goal is to reconstruct a low-rank model representative of the vertical acoustic-induced velocity, only the decompositions of this velocity component are shown and commented.

4.1. Energy distribution between the modes and spectra

The energy distribution of POD modes, the correlation strength between the modes for CCD, and the spectra of the coefficients $c_k(t)$ are reported in Figs. 3 and 4 for both SPLs and Mach numbers. The center column represents the 130 dB case, while the right column represents the 145dB case. The SPOD spectra provide the modes' energetic content and frequency distribution. The forcing frequency at 1.4 kHz, its first harmonic, and the cavity mode at 14 kHz are highlighted in the figures.

The normalized percentage of energy and correlation strength associated with POD and CCD modes for the case with $M = 0$ is shown in Fig. 3(a) and (d) for the first 50 modes. The first three POD modes (Fig. 3(a)) account for more than 50 % of the turbulent kinetic energy. The percentage of energy associated with the first two modes is larger at 130 dB. This can be attributed to stronger non-linear effects in higher-order modes when the acoustic wave amplitude is 145 dB. Consequently, more modes are needed to reconstruct the acoustic-induced flow field.

The correlation strength distribution between the CCD modes (Fig. 3(d)), on the other hand, exhibits a much quicker decay than the POD ones; higher-order modes beyond the third account for less than 2 % of those of the first two modes. A slight difference in the correlation strength exists between the third and fourth modes; similarly to the POD case, their contribution at 145 dB is larger

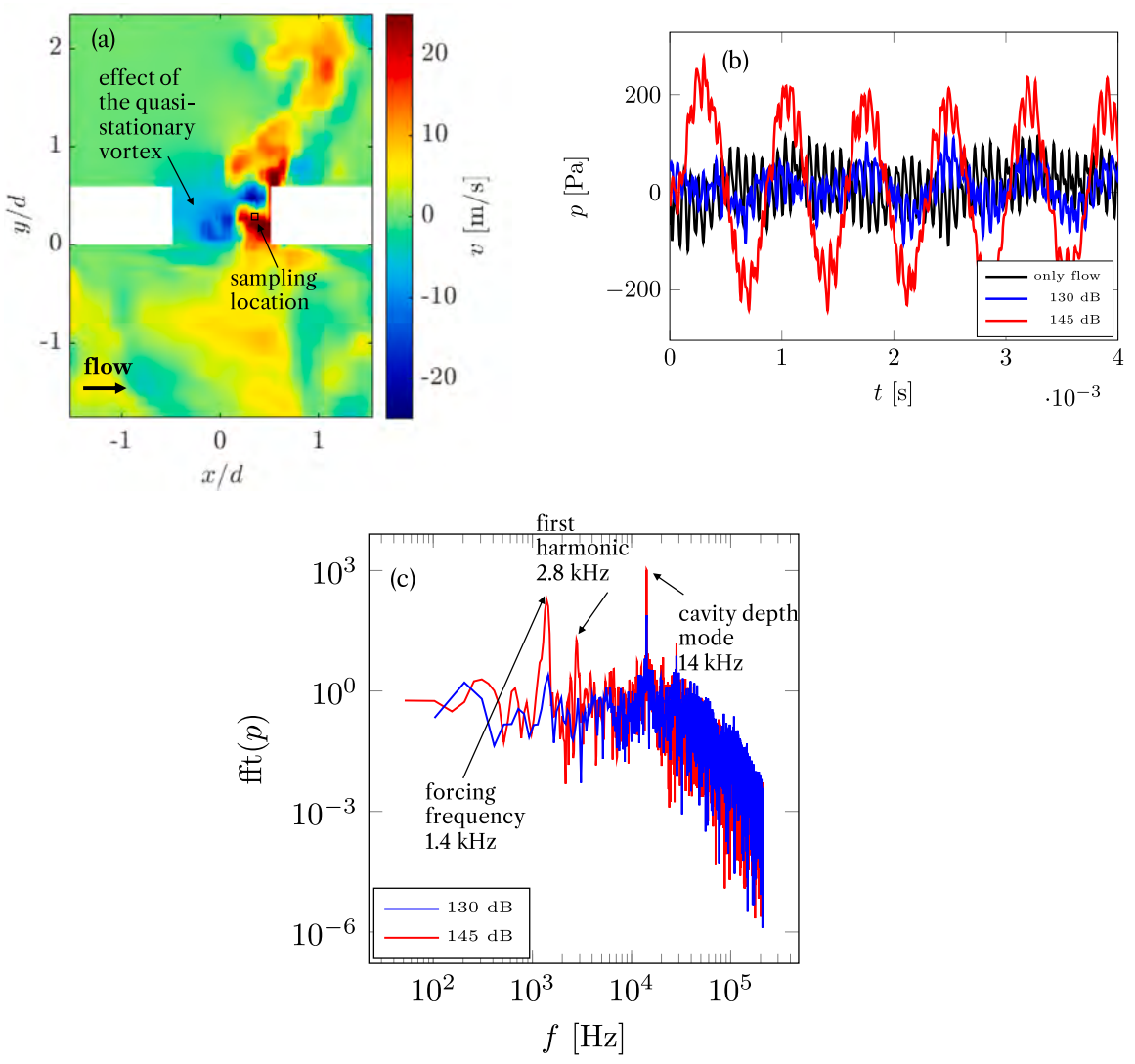

Fig. 2. (a) Contour of the unfiltered vertical velocity fluctuation, randomly chosen snapshot for the case $M = 0.32$ and SPL 145 dB, (b) pressure fluctuations in the vicinity of an orifice, comparison between no acoustic source case and acoustic source at 130 dB and 145 dB, (c) spectrum of the pressure fluctuations in the orifice, comparison between 130 dB and 145 dB at $M = 0.32$.

than that at 130 dB due to non-linear effects. This suggests that only the first few modes correlate well with the upstream acoustic forcing, whereas high-order modes do not, which is likely due to flow non-linearities.

The spectra of the coefficients obtained from POD and CCD are shown in Fig. 3(b), (c), (e), (f). For the no-flow case, for both SPLs, the coefficients of the first POD and CCD modes capture the dominant flow structures at the forcing frequency 1.4 kHz. When forcing a system at a certain frequency, any response at a different frequency can be considered a non-linear response. Therefore, harmonics of 1.4 kHz, especially the first at 2.8 kHz, are representative of non-linearities. These frequencies are captured mainly by the third mode.

The SPOD energy-frequency spectra (where λ_j is the energy associated to the $j-$mode) for the first three modes are reported in Fig. 3 for the 130 dB (g) and 145 dB (h) cases without grazing flow. The SPOD spectrum evidences a low-rank behavior at the forcing frequency and its harmonics, with the energy of the first mode being two orders of magnitude larger than the second at 1.4 kHz. As the duration of the signal is limited, the convergence of the decomposition methods is impacted. For this reason, the low-rank property presented should be taken with caution. Note that the harmonics are spread between all the SPOD modes. As for the previous decomposition methods, the non-linear response is more pronounced at 145 dB, as indicated by the stronger harmonics, which are about one order of magnitude smaller than the peak at the fundamental frequency. At 130 dB, harmonics are visible but remain more than two orders of magnitude weaker, confirming that the flow is largely linear. A weak broadband contribution, negligible at 130 dB (over five orders of magnitude smaller than the one at the fundamental frequency), slightly increases at 145 dB due to

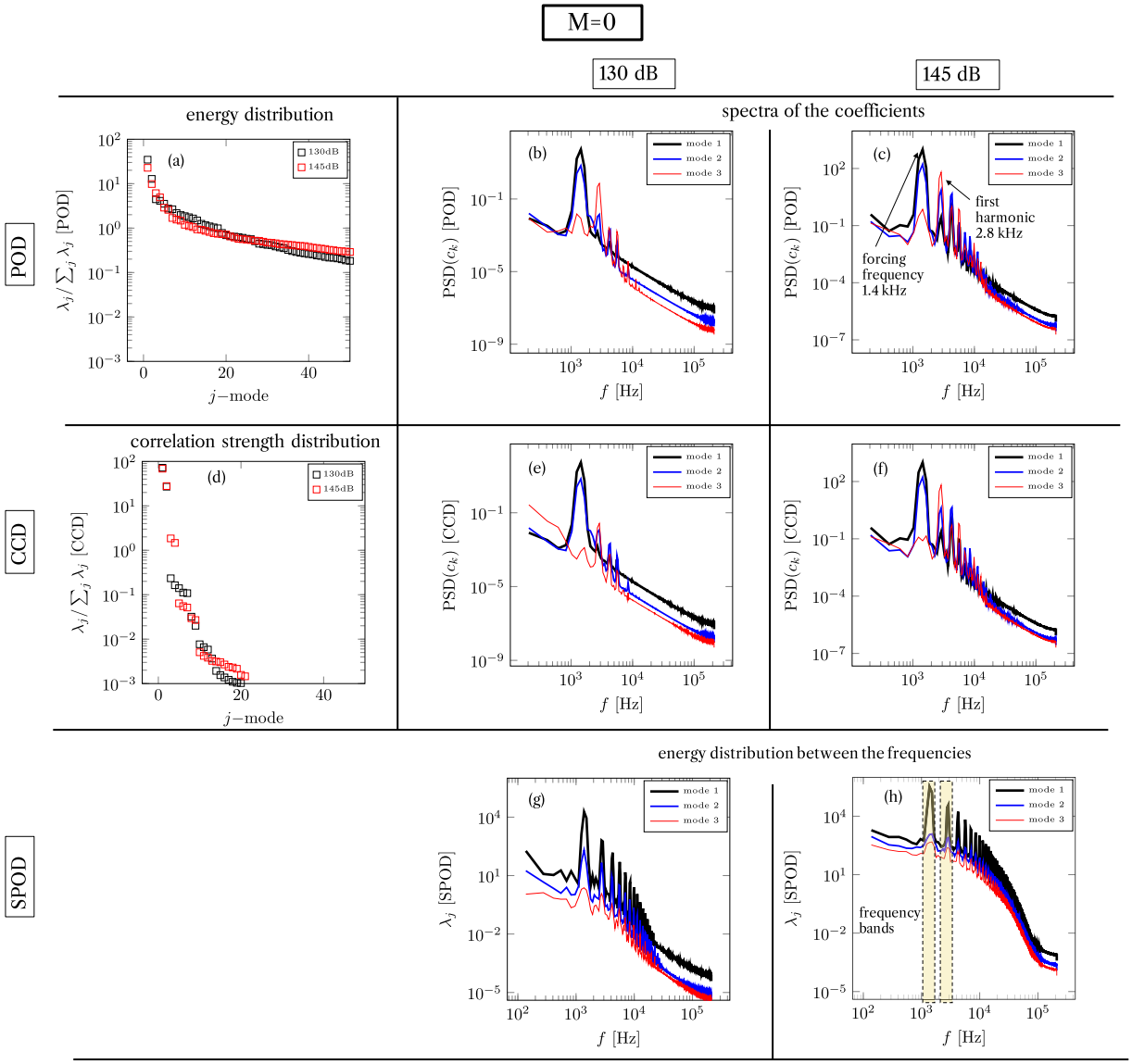

Fig. 3. Fraction of the energy for POD (a) and correlation energy between the modes for CCD (d). PSD of the decomposition coefficients of the first three modes for POD (b-c), CCD (e-f), and SPOD spectra (g-h). Results at $M = 0$ comparison between 130 and 145 dB.

turbulence generated by vortex shedding near the cavity orifice. Since the SPOD method decomposes the flow structures at a fixed frequency into multiple modes, reconstructing the field using only a single frequency band (even with multiple modes) will not include non-linearities reflected by other frequencies. To include them, SPOD modes at harmonic frequencies must be considered.

The normalized percentage of energy and correlation strength distribution between the modes for the cases with grazing flow are shown in Fig. 4(a) and (d). POD results (a) show a less marked low-rank behavior than without grazing flow. The first two modes account for less than 10 % of the total energy for both SPLs. This is due to the presence of turbulence close to the walls, and it is further accentuated by the self-tone at 14 kHz, which acts as a disturbing factor in the modal decompositions.

Conversely, the CCD correlation energy distribution (Fig. 4(d)) exhibits a quick-decaying behavior even in the presence of the grazing flow. High-order modes are almost one order of magnitude lower than the first two modes. This means that although the system exhibits higher degrees of freedom compared to the $M = 0$ case, the number of modes significantly correlated with acoustic forcing is still low. In this sense, CCD is more suitable than POD in diagnosing the acoustically-driven flow since it targets the upstream forcing-correlated flow structures. The low-rank behavior is further accentuated when the SPL is larger, as the AHFR increases.

The spectra of the coefficients of the POD and CCD modes are reported in Fig. 4(b), (c), (e), (f). The energy distribution between frequencies, obtained with the SPOD method (g,h), for the two SPLs is also reported in the same figure. When introducing the grazing flow, spectra are dominated by the broadband effect of the turbulence at low frequencies. At 130 dB, the peak at the forcing acoustic

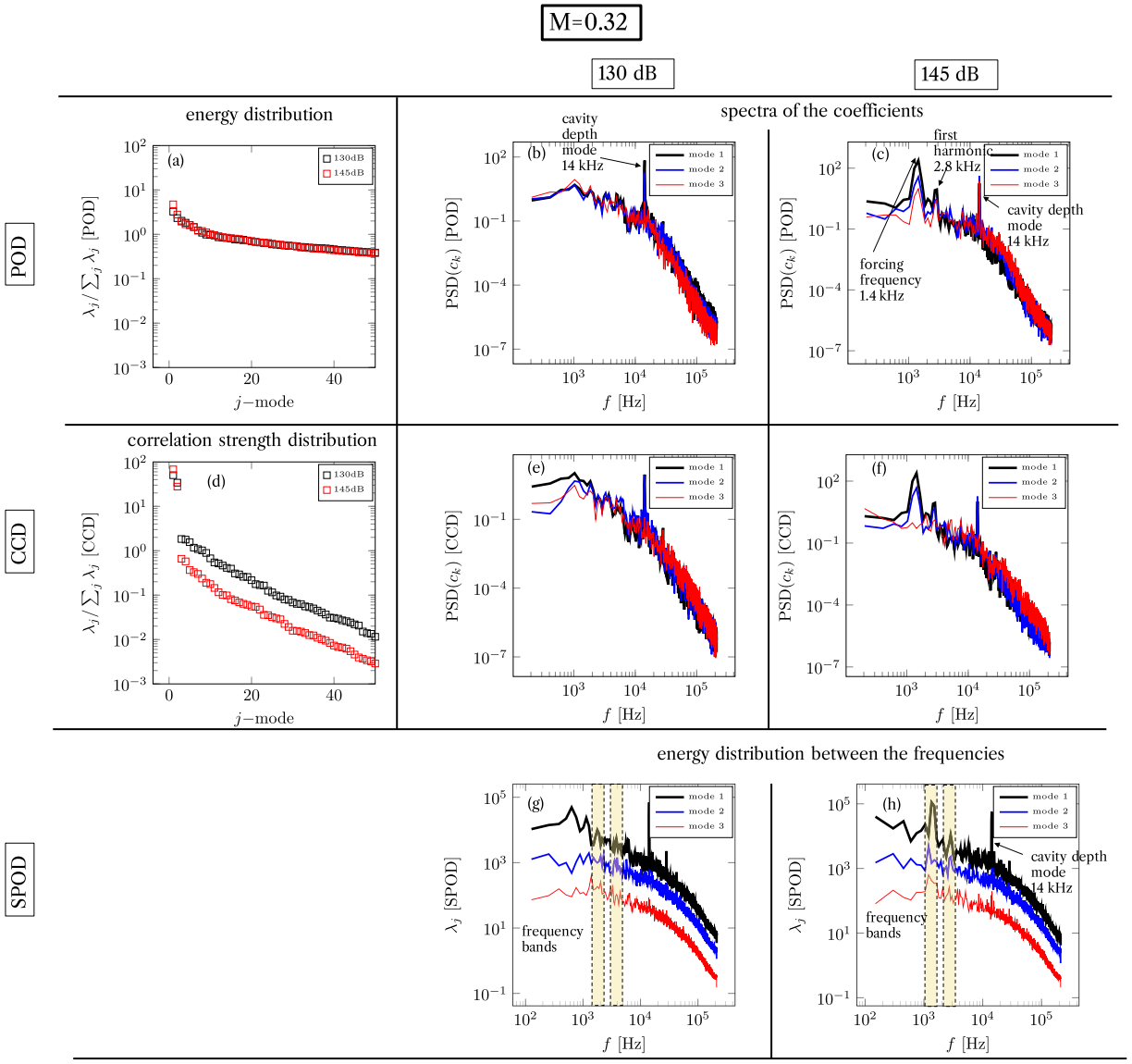

Fig. 4. Fraction of the energy for POD (a) and correlation energy for CCD (d) between the modes. PSD of the decomposition coefficients of the first three modes for POD (b-c), CCD (e-f), and SPOD spectra (g-h). Results at $M = 0.32$ comparison between 130 and 145 dB.

frequency does not emerge in all the spectra, but it is visible when increasing the SPL to 145 dB. At 130 dB the coefficients of the first and second POD modes have a predominant component at the self-oscillating tone at 14 kHz. This suggests that the POD method does not correctly extract the acoustic-induced velocity associated with the forcing frequency. This is because the POD modes are dominated by the significant energy of the tone at 14 kHz. As the source tone at 1.4 kHz does not emerge from the turbulence level at 130 dB, due to the limited AHFR, the SPOD method works only if the forcing frequency is known a priori.

For these reasons, the energetic distribution between the modes and the spectra of their coefficients, which provide the temporal evolution of the mode, are not sufficient to fully discern which of the modes contributes to the acoustic-induced velocity. Consequently, an inspection of the mode contours, which provide the spatial distribution of the mode, is necessary, and it will be tackled in the following subsection.

4.2. Contours and modes shapes for POD, CCD, and SPOD

Contours of the first three modes of the vertical velocity component obtained with POD, CCD and the ones for the first two modes at 1.4 kHz and the first mode at 2.8 kHz obtained applying SPOD are shown in Figs. 5 and 6 for the case without flow and in the Figs. 7 and 8 in the presence of the grazing flow at $M = 0.32$.

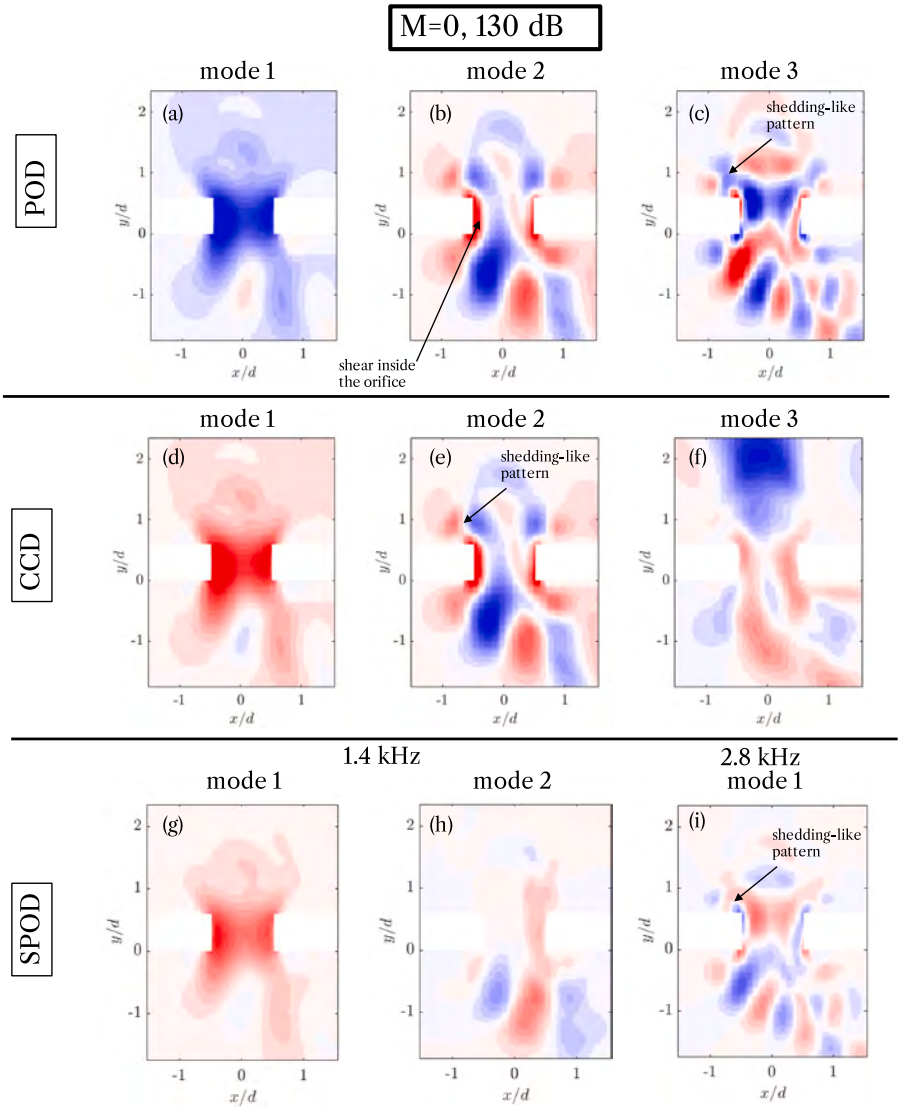

Fig. 5. Contour of the first, second and third mode, $M = 0$ acoustic source at 1.4 kHz and SPL = 130 dB, (a-c) POD, (d-f) CCD and (g-i) SPOD.

The first modes, obtained with all the decomposition techniques, are similar in the absence of grazing flow and acoustic wave amplitude equal to 130 dB. The first mode represents the flow entering the orifice due to the acoustic forcing. The second mode represents the shear forming on the side walls of the orifice because of the acoustic-induced flow. Inside and outside the orifice, positive and negative values might be associated with weak shedding, which can be related to weak non-linearity as expected for this case. This pattern is also visible in the third mode obtained from POD and CCD. It is interesting to notice that the pattern found in the second and third modes is similar to the first SPOD mode at 2.8 kHz, thus confirming that it can be associated with weak non-linearities. This highlights the capability of the SPOD technique to distinguish non-linearities associated with the acoustic forcing.

Increasing the amplitude of the acoustic excitation to 145 dB, still in the absence of grazing flow, the shape of the first mode, associated with the acoustic-induced flow inside the orifice, is identical for the three decomposition methods. One can easily notice that within the orifice, the energy distribution is more uniform than for the first mode at 130 dB (Fig. 5) and that regions with high energy expand more above and below the face sheet when increasing the SPL. The second POD and CCD modes indicate, as happens for 130 dB, the contribution of the shear layer and the shedding to the vertical velocity. In this case, two relevant observations shall be made: the asymmetry between the upstream and downstream edges of the orifice is enhanced, and the intensity and size of the shed vortices are higher. Similar observations can be made by looking at the results from the SPOD technique. However, in this case, the extension of the highly energetic region above and below the face sheet is smaller, and, for the first mode at 1.4 kHz, a highly

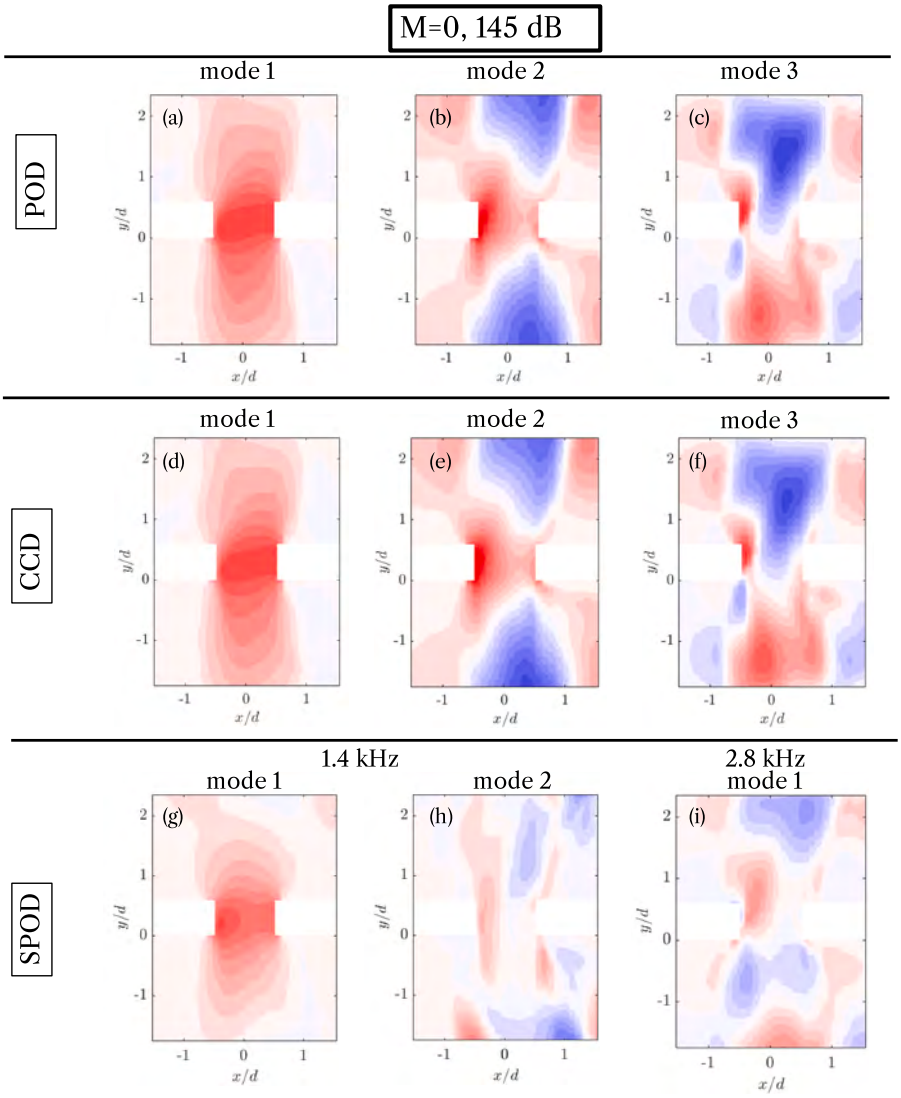

Fig. 6. Contour of the first, second and third mode, $M = 0$ acoustic source at 1.4 kHz and SPL = 145 dB, (a-c) POD, (d-f) CCD and (g-i) SPOD.

energetic area can be seen at the upstream edge of the orifice. Also, the first mode at 2.8 kHz shows the vorticity associated with the non-linearities, while the second mode at 1.4 kHz mostly highlights shear effects at the edge of the shedding area.

When introducing the grazing flow (Fig. 7), considering the acoustic wave with amplitude of 130 dB, the mode shape shall reflect the modification that the acoustic-induced flow undergoes due to the quasi-stationary vortex in the first half of the orifice [5]. This reduction of the equivalent porosity and the presence of a localized jet in the downstream edge of the orifice are well visible in both the CCD and SPOD first and second modes (Fig. 7 (d) and (g)). However, the CCD mode contours exhibit residual traces of turbulent motion, which, in agreement with the spectra shown in Fig. 4, confirms that the mode is not purely associated with the acoustic forcing. The jet-like flow topology is not well visible in the first two modes obtained with the POD technique (Fig. 7(a) and (b)) while it appears in the third mode (Fig. 7(c)). As POD maximizes the turbulent kinetic energy, the first two modes at 130 dB capture the self-excited tone at 14 kHz, which is stronger than the flow dynamics linked with the acoustic-generated flow at 1.4 kHz. This provides the visual confirmation of the results discussed by looking at the spectra of the coefficients in Fig. 4(b). The mode's shape is similar to the structure educed from DMD by Brunner et al. [19], consisting of a vortex detached from the upstream edge of the orifice and another colliding with the downstream edge. The authors associated this behaviour with a feedback loop tone oscillation, akin to a Rossiter mode, which leads to an increase in turbulent kinetic energy.

The first SPOD mode at 2.8 kHz doesn't exhibit any jet-like pattern; this confirms that, at low SPL, the non-linearities are due to the flow rather than the effect of the harmonics of the source frequency.

Increasing the SPL to 145 dB in the presence of grazing flow, the AHFR increases. For this reason, the turbulent kinetic energy associated with the acoustic-induced flow dominates the self-tone at 14 kHz. This is reflected in the shape of the first mode, which,

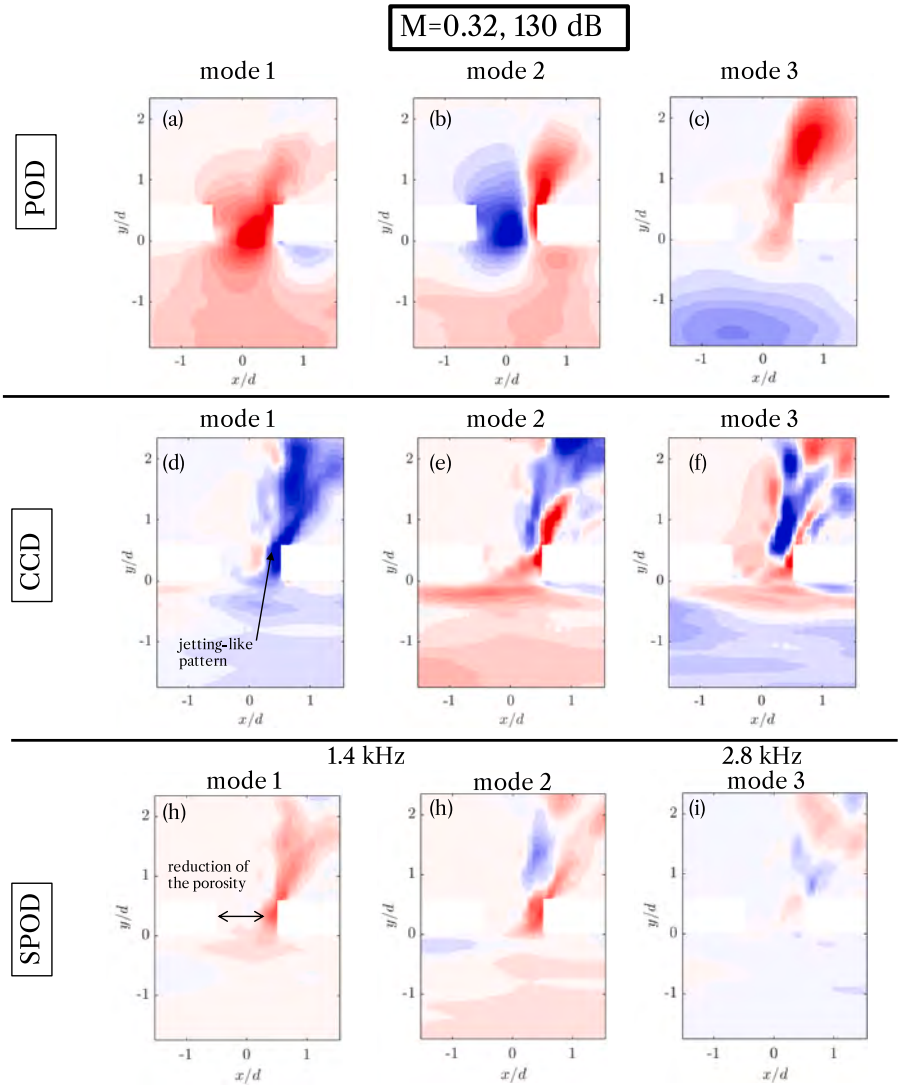

Fig. 7. Contour of the first, second and third mode, $M = 0.3$ acoustic source at 1.4 kHz and SPL = 130 dB, (a-c) POD, (d-f) CCD and (g-i) SPOD.

in this case, is the same for all the decomposition techniques. The contours clearly show the formation of a jet-like flow in the downstream edge of the orifice. This jet-like pattern is more extended inside the liner's cavity for the 145 dB case than the 130 dB one.

One can notice that the second and third modes for the POD results (Fig. 8(b) and (c)) are identical to the first two modes at 130 dB indicating that these two modes represent the self-tone at 14 kHz which is present in the presence of grazing flow for this specific geometry. At 145 dB, looking at the results from the CCD technique, a coherent pattern that resembles a jet appears in all the modes. The first SPOD mode at 2.8 kHz has a jet-like shape, suggesting that, as the SPL increases, the non-linear effects due to the high acoustic forcing harmonics are not negligible and are not entirely dominated by the grazing flow, as it happens for 130 dB.

5. Reconstructed acoustic-induced velocity fields

5.1. Contours of the reconstructed vertical acoustic-induced velocity

Contours of the normalized value of the amplitude of the reconstructed vertical acoustic-induced velocity fluctuations are reported in Figs. 9 and 10 for the conditions without grazing flow and Figs. 11 and in 12 for these at $M = 0.32$. For brevity, the contours reported are all related to the inflow phase ($\phi = \pi/2$). Along with the reconstructed acoustic-induced velocity from the modal decompositions, a snapshot of the instantaneous vertical velocity field in the inflow phase is also reported. It is clear that, in the presence of grazing

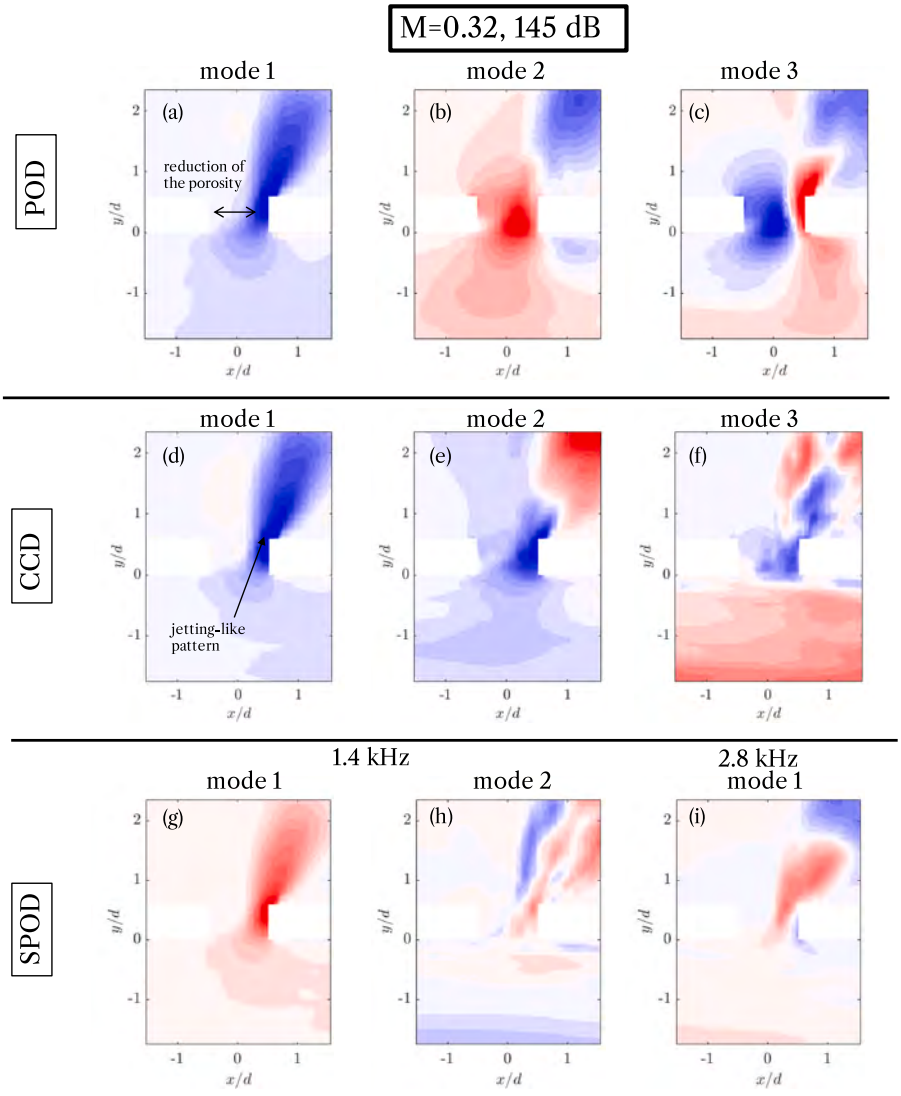

Fig. 8. Contour of the first, second and third mode, $M = 0.3$, acoustic source at 1.4 kHz and SPL = 145 dB, (a-c) POD, (d-f) CCD and (g-i) SPOD.

flow, the velocity field is polluted by turbulent fluctuations in the vicinity of the orifice. Furthermore, the results obtained with the triple decomposition are also reported.

Starting from the case without grazing flow and amplitude of the plane acoustic wave equal to 130 dB (Fig. 9), it can be noted that, as expected, all the methods reconstruct well the raw signal using only one mode. Adding additional modes does not show relevant changes because of the weak non-linearities present in this case.

Increasing the SPL to 145 dB (Fig. 12), the shape of the acoustic-induced velocity contour changes. The raw signal evidences an asymmetry between the upstream and downstream edges of the orifice, due to the grazing acoustic wave, and a roll-up inside the cavity due to the formation of a vortex. While the triple decomposition shows the vortex roll-up, CCD and POD, even adding the first three modes, do not show this feature. Results from the SPOD, instead, show that the acoustic-induced field is similar to the one obtained from CCD and POD, if only a band centered at the excitation frequency is considered.

Adding more modes identifies where the small non-linearities are present: they are concentrated in the middle of the face sheet thickness, predominantly on the upstream edge of the orifice. This conclusion is mainly supported by Fig. 10, where the contributions of two bands of the first mode obtained from the SPOD technique, centered at 1.4 kHz and 2.8 kHz, are reported. Furthermore, SPOD shows hints of vortex roll-up, even if not as strong as the one obtained from the triple decomposition. This may indicate that the triple decomposition includes high-order features not associated with the acoustic excitation frequency and first harmonic.

Obtaining the acoustic-induced velocity field is less trivial in the presence of grazing flow. There are substantial differences between the methods for the case with acoustic amplitude equal to 130 dB (Fig. 11). First, the triple decomposition and the POD do not show the formation of the jet-like motion in the downstream edge of the orifice, but a localized spot of high velocity towards $y/d = 0$.

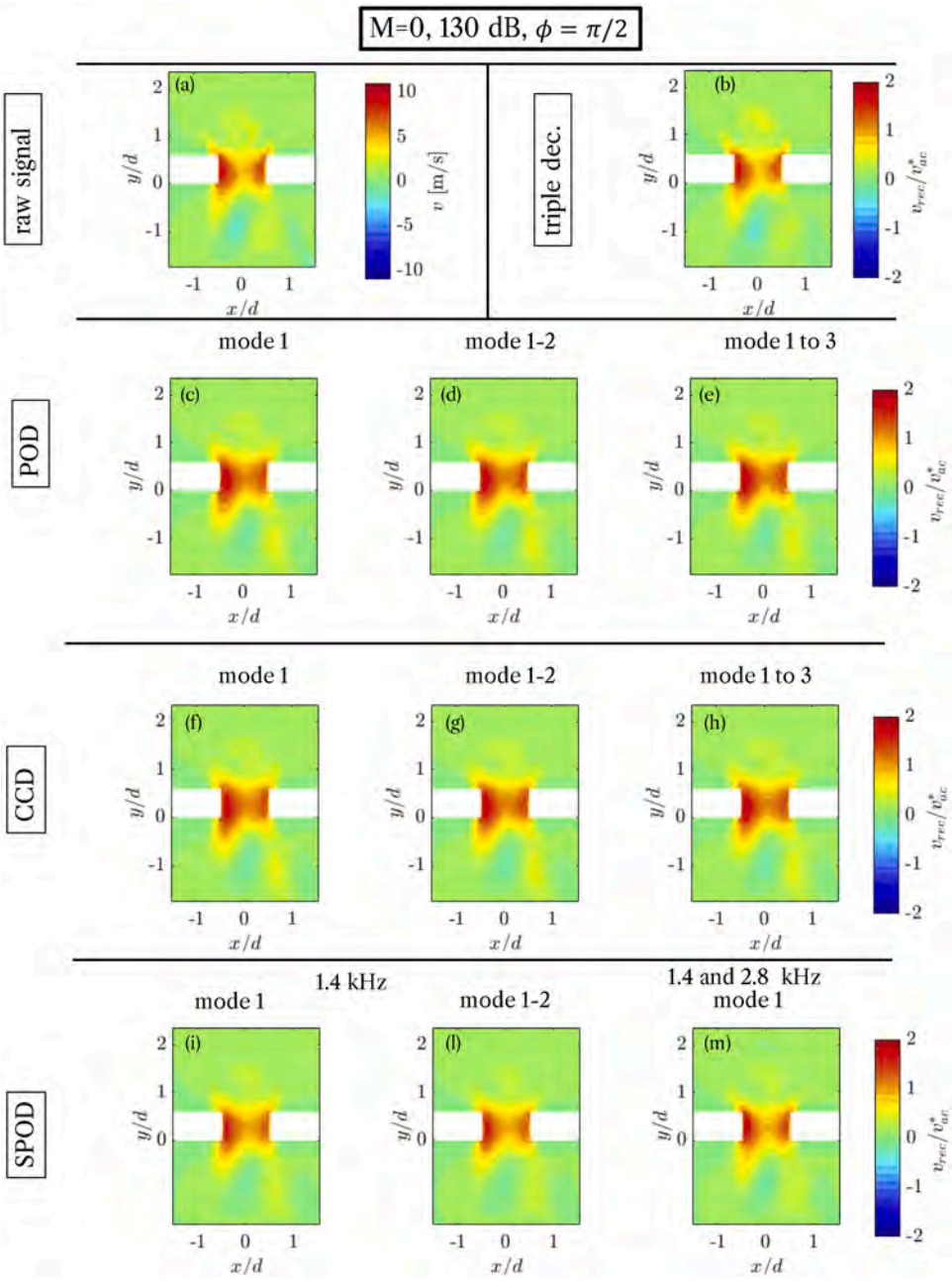

Fig. 9. Contour of the reconstructed vertical velocity fluctuation, v in the inflow phase, $M = 0$ and SPL = 130 dB, (a) raw data, (b) triple decomposition, (c-e) POD, (f-h) CCD, (i-m) SPOD.

This may be caused by the contribution of the high-intensity acoustic wave with a tonal frequency equal to 14 kHz. Results from the CCD technique provide the expected flow structures, but with a magnitude larger than the one obtained using the SPOD technique. However, assessing which of the two is the best is difficult. The only observation that can be made is that the results obtained from the SPOD, using only one or two frequency bands, show the amplitude of the acoustic-induced vertical velocity component that is closer to the expected theoretical value in the absence of flow [40]. This might hint that SPOD is better capable of obtaining the correct acoustic-induced velocity field.

Increasing the amplitude of the acoustic wave reduces the differences between the results obtained with different methods. The triple decomposition, distinct from the modal decomposition methods, shows traces of vorticity within the cavity that might be attributed to the dominant 14 kHz cavity mode. The modal decomposition results show a clear region of high velocity at the downstream

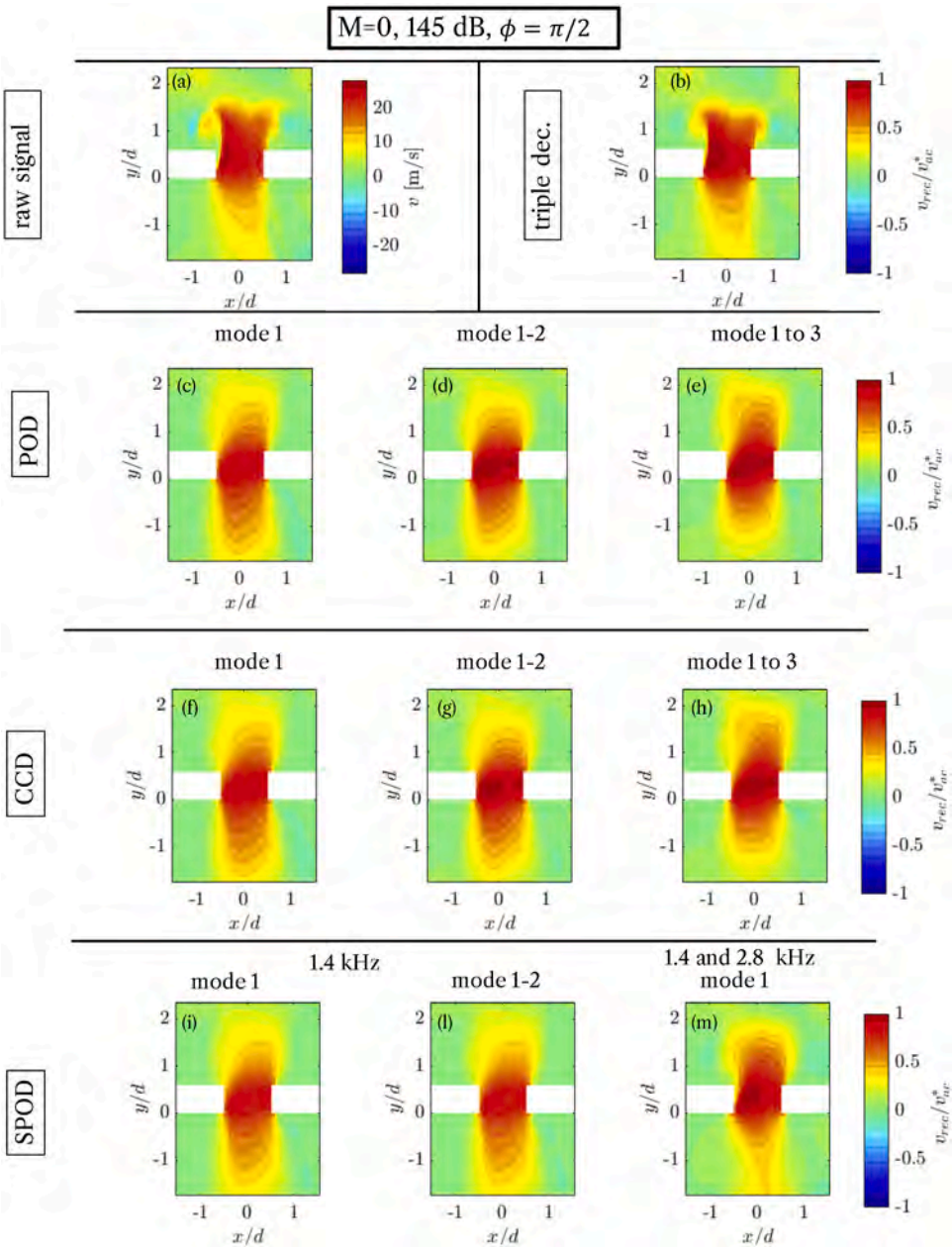

Fig. 10. Contour of the reconstructed vertical velocity fluctuation, v, in the inflow phase, $M = 0$ and SPL$=$ 145 dB, (a) raw data, (b) triple decomposition, (c-e) POD, (f-h) CCD, (i-m) SPOD.

edge of the orifice, but, as for the case at 130 dB, SPOD results, independently of the number of bands included in the reconstruction, show lower velocity amplitude and closer to the one predicted by Morse et al. [40].

5.2. Time series of the reconstructed vertical acoustic-induced velocity in the presence of grazing flow

To better highlight the effect of changing the number of modes in the reconstruction of the instantaneous acoustic-induced velocity in the presence of flow, the time series, over the entire cycle, of the reconstructed acoustic-induced vertical velocity within the orifice, sampled at the location shown in Fig. 1(c), is reported in Fig. 13 for both SPLs. The time cycle is expressed as the phase ϕ that varies between 0 to 2π. The inflow phase is at $\phi = \pi/2$ and the outflow one at $\phi = 3\pi/2$. The left column reports the results at 130 dB and the right column the ones at 145 dB.

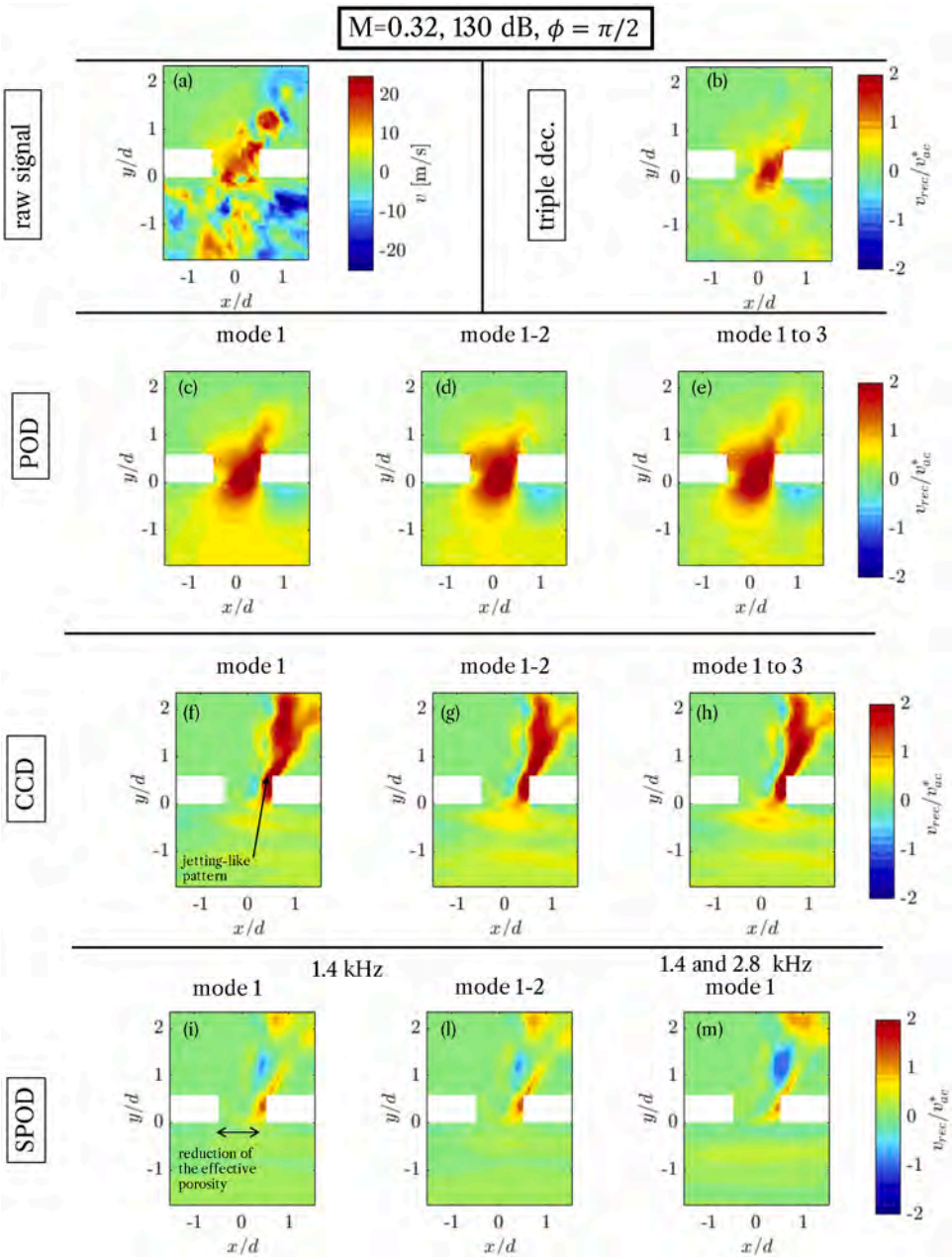

Fig. 11. Contour of the reconstructed vertical velocity fluctuation, v, in the inflow phase, $M = 0.32$ and SPL = 130 dB, (a) raw data, (b) triple decomposition, (c-e) POD, (f-h) CCD, (i-m) SPOD.

For all the cases, the raw time series show the dominant acoustic depth mode at 14 kHz, and, for the case at 130 dB, the sinusoidal modulation at 1.4 kHz is hardly visible. The consequence is that none of the reconstruction approaches, except the SPOD technique, can reconstruct the expected sinusoidal signal. This is expected for the SPOD method based on what was discussed previously when describing the spectral content of the temporal coefficient. The triple decomposition fails to reconstruct the periodic motion maybe because of the short simulation time. This observation strengthens the relevance of adopting advanced reconstruction methods to extract the acoustic-induced velocity in the presence of unwanted coherent noise sources.

As the SPL increases to 145 dB and the acoustic wave becomes energetically stronger, the periodic motion is well obtained by all the applied techniques (Fig. 13(b), (d), (f), (h)). As for the previous case, the tonal noise at 14 kHz is still present for all the techniques but the SPOD (Fig. 13 (e) and (f)). Even the CCD, which enforces the correlation with the reference pressure signal, does not fully remove the 14 kHz contribution.

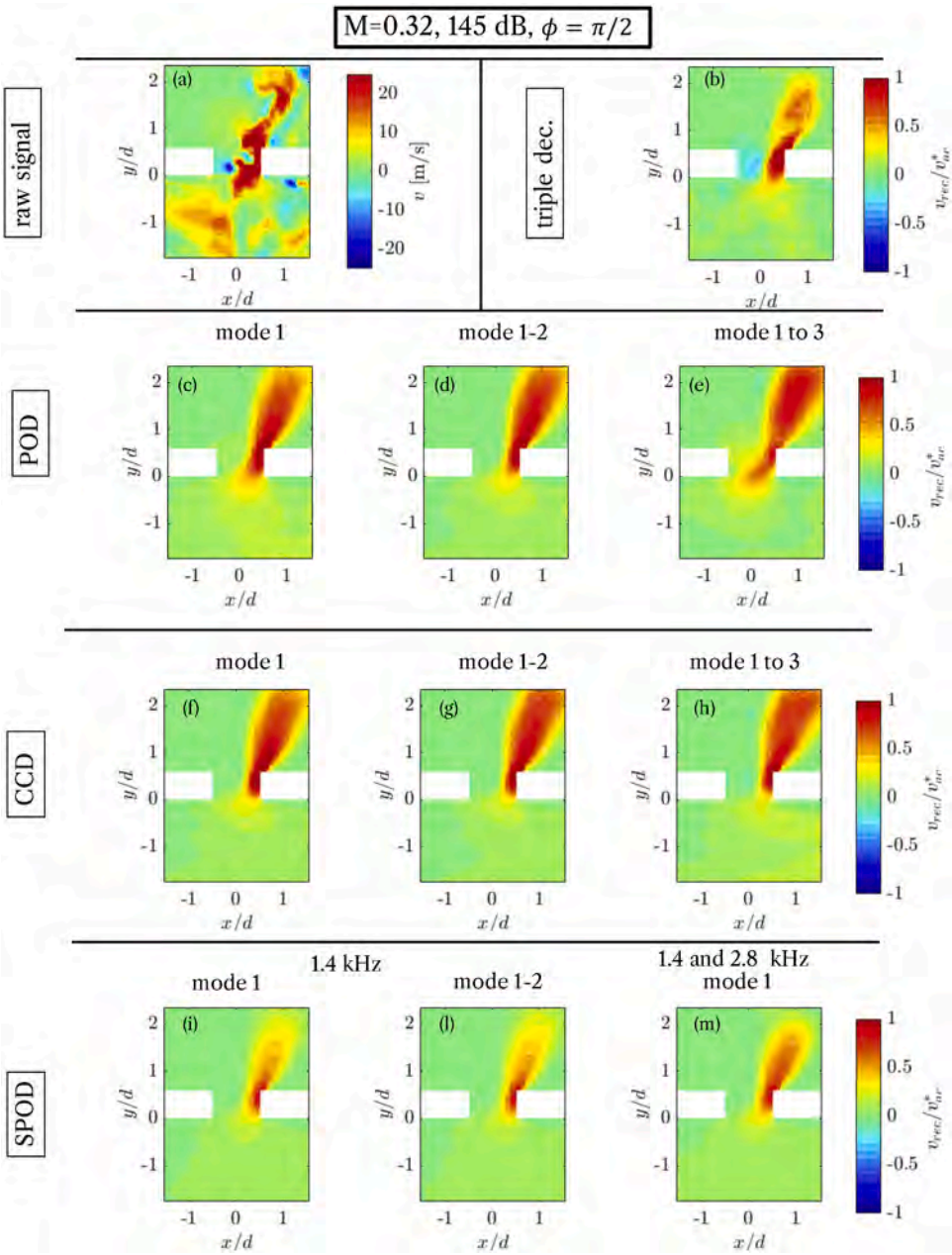

Fig. 12. Contour of the reconstructed vertical velocity fluctuation, v, in the inflow phase, $M = 0.32$ and SPL$=$ 145 dB, (a) raw data, (b) triple decomposition, (c-e) POD, (f-h) CCD, (i-m) SPOD.

5.3. Acoustic-induced velocity profiles in the orifice at varying phases

In Fig. 14 the acoustic velocity profiles, obtained in the middle of the orifice thickness, are shown for the no-flow condition at four phases: $\phi = 0, \pi/2, \pi, 3\pi/2$. The effect of changing the number of modes in the reduced order model is also reported. At 130 dB (left column), varying the number of modes has a negligible impact on the inflow and outflow phases, while it has an impact on the phases $\phi = 0$ and π. Adding the contribution at 2.8 kHz in the SPOD slightly increases the acoustic velocity for all the phases. The velocity profiles for the 130 dB case are not symmetric in the streamwise direction, with a larger velocity in correspondence with the upstream corner of the orifice, which is expected because the acoustic wave is grazing.

At 145 dB the profile exhibits a less significant asymmetry in the streamwise direction. However, as the non-linearities are stronger at 145 dB, the magnitude of the reconstructed velocity profiles is affected by the number of selected modes. Adding the second and

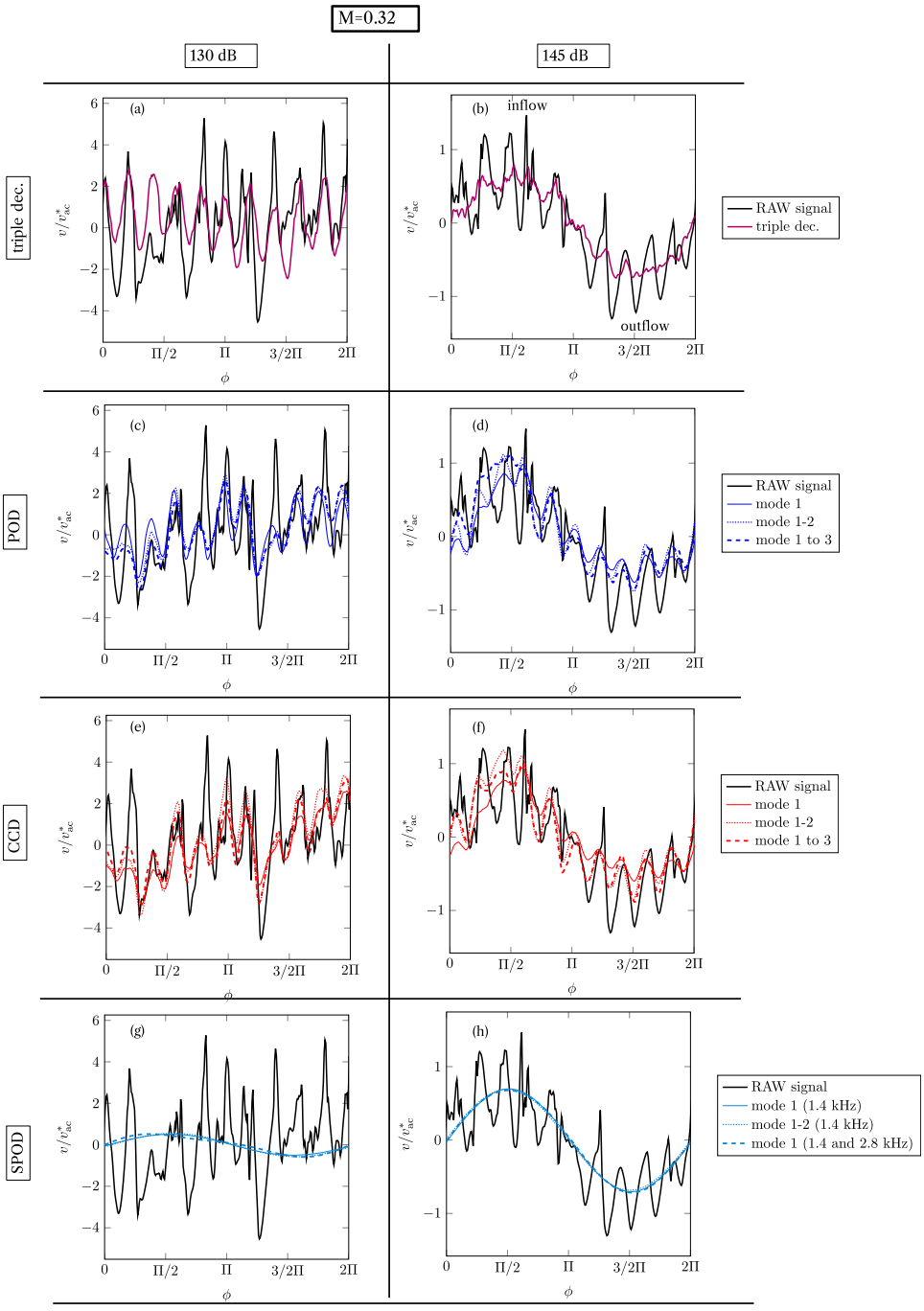

Fig. 13. Portion of the time-series of the vertical velocity probed at the location shown in Fig. 1(c), raw time series and reconstructed time series using triple decomposition (a-b), POD (c-d), CCD (e-f), SPOD (g-h), (a-c-e) 130 dB, (b-d-f-h) 145 dB.

third modes or considering the harmonic at 2.8 kHz causes an increase in the reconstructed acoustic-induced velocity profile at the upstream edge of the orifice.

The acoustic-induced vertical velocity profiles in the presence of grazing flow are shown in Fig. 15. The presence of the grazing turbulent flow generates a clear streamwise asymmetry in the inflow and outflow acoustic-induced velocity profile. Despite the maximum value being similar to the no-flow case, in the first half of the cavity, the vertical velocity is small, in agreement with the presence of a quasi-steady vortex reported by several authors [6,26].

When the amplitude of the grazing acoustic wave is low, the acoustic profiles obtained with the different decomposition methods are different. This indicates a higher complexity and lower reliability in the decomposition of acoustic and aerodynamic fields at a

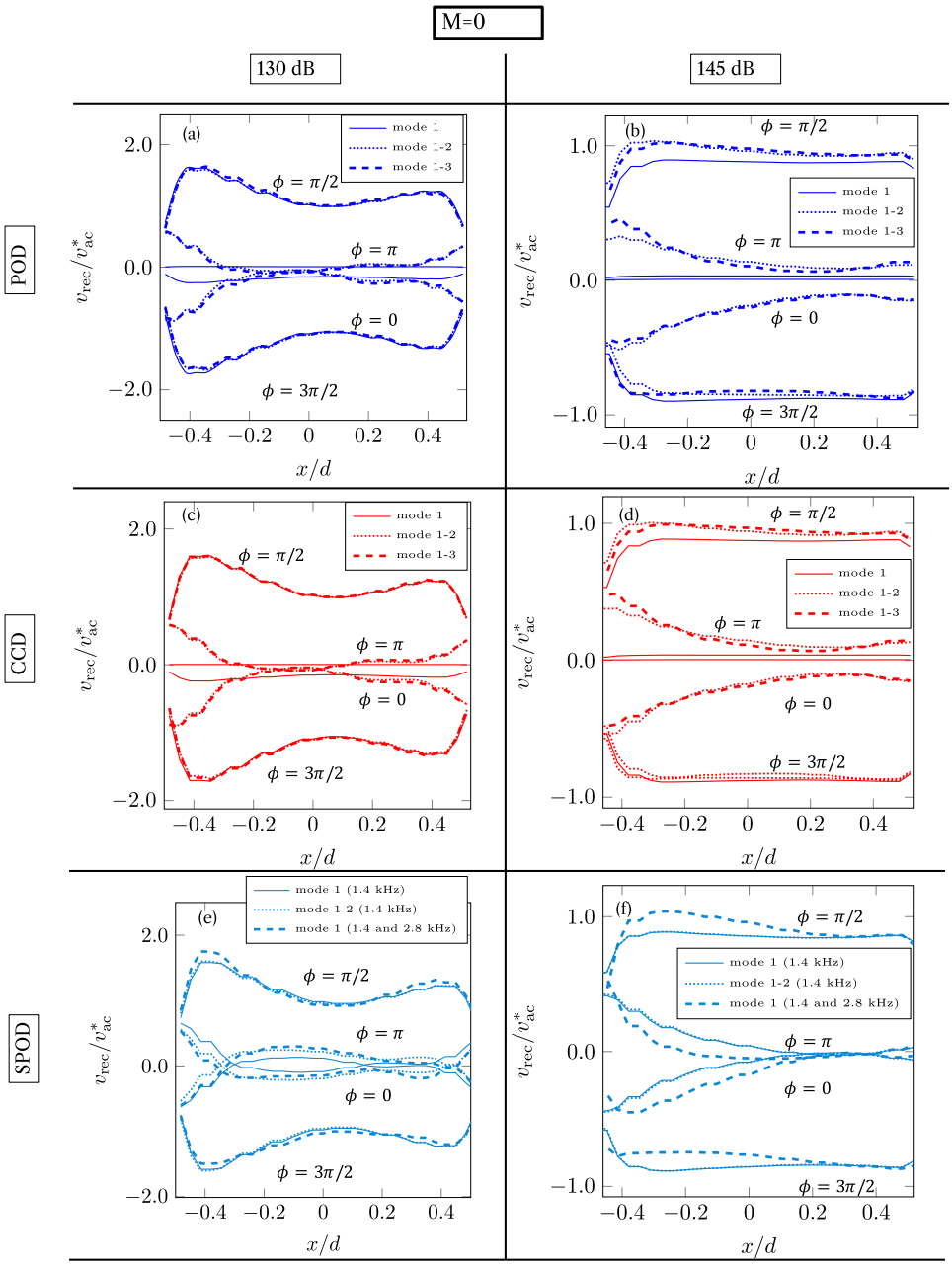

Fig. 14. Reconstructed vertical velocity profiles at the center-line of the orifice using POD (a-b), CCD (c-d), and SPOD (e-f) at $M = 0$, left column 130 dB, right column 145 dB. The impact of the number of modes used for the reconstruction and the frequency band (SPOD) for different phases ϕ is reported.

lower acoustic-to-hydrodynamic fluctuation ratio. As shown by the contour of the modes, and confirmed here for the four phases selected, the POD results are influenced by the peak at 14 kHz that dominates the acoustic velocity. For this reason, the profile exhibits a non-negligible vertical velocity in the upstream portion of the orifice in both inflow and outflow phases, but also at $\phi = 0$ and $\phi = \pi$. Based on the existing literature, this behavior is not expected. The SPOD and CCD results are similar in shape, but the maximum value of the acoustic velocity reconstructed with CCD is double the one reconstructed with SPOD.

5.4. Convection velocity estimation from the residual pressure field

The residual pressure fields are analyzed by evaluating the convection velocity. This is done to verify that the residual field contains only hydrodynamic fluctuations. The residual pressure field is defined as the difference between the raw pressure signal and the reconstructed pressure (Eq. (10)) using the same ROM approach as done earlier for the vertical velocity

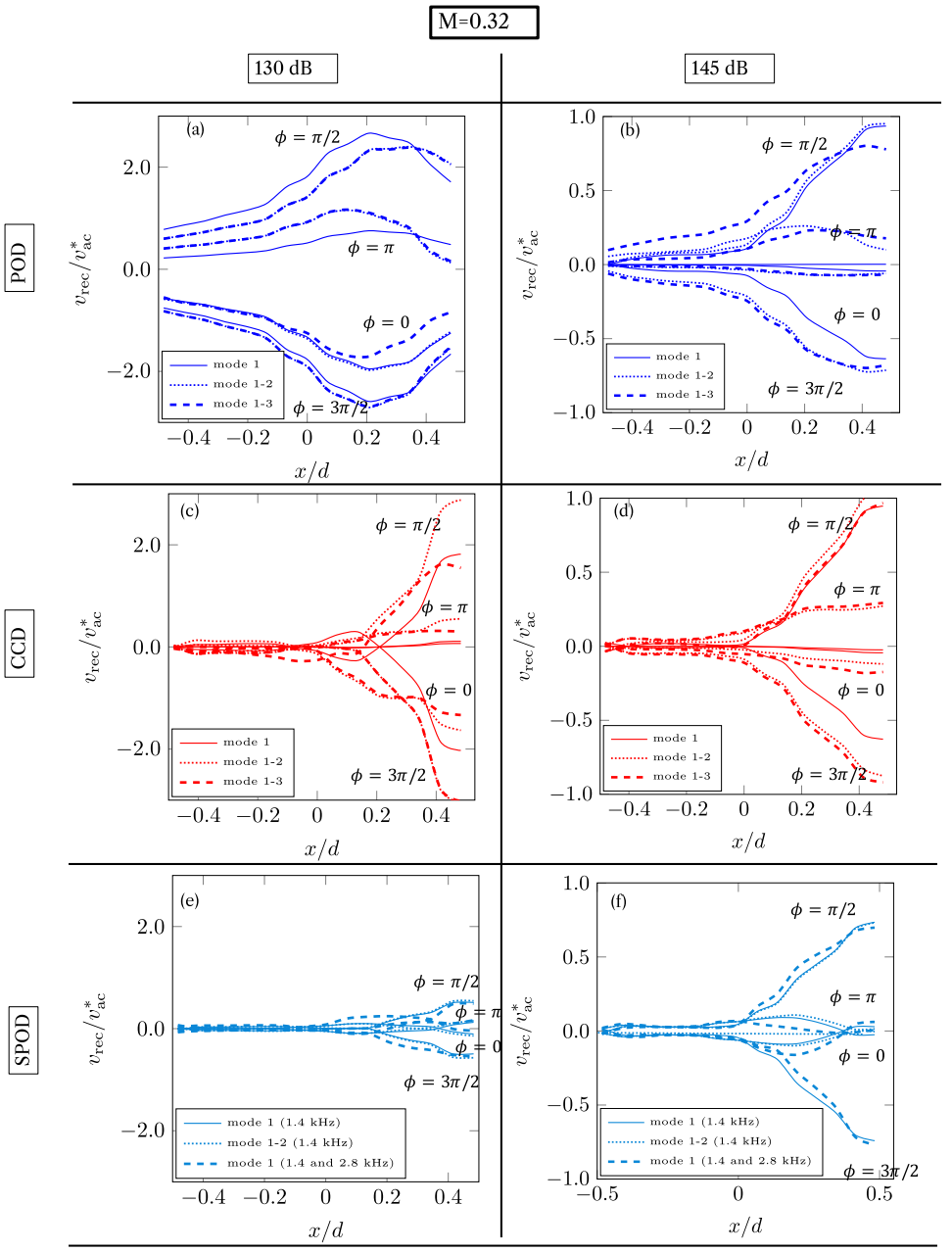

Fig. 15. Reconstructed vertical velocity profiles at the center-line of the orifice using POD (a-b), CCD (c-d), and SPOD (e-f) at $M = 0.32$, left column 130 dB, right column 145 dB. The impact of the number of modes used for the reconstruction and the frequency band (SPOD) for different phases ϕ is reported.

component.

$$p_{\mathrm{res}}(t) = p(t) - p_{\mathrm{rec}}(t). \tag{10}$$

The time series of p_{res} is evaluated at the two points indicated in Fig. 1(c). These two point locations are chosen because, at that wall-normal location, the grazing flow velocity is not negligible. The convection velocity is then obtained by locating the dominant peak in the cross-correlation between the two residual signals [41] because it represents the time a turbulent eddy takes to travel from the point P_1 to the point P_2. This time difference is converted into a velocity, knowing the distance between the two points. This velocity is the convection velocity of the turbulent eddies U_c.

In Fig. 16(a) and (b), the normalized cross-correlation is shown as a function of the convection velocity for the three modal decomposition techniques at 130 and 145 dB. The effect of changing the number of modes for POD and CCD and the frequency band

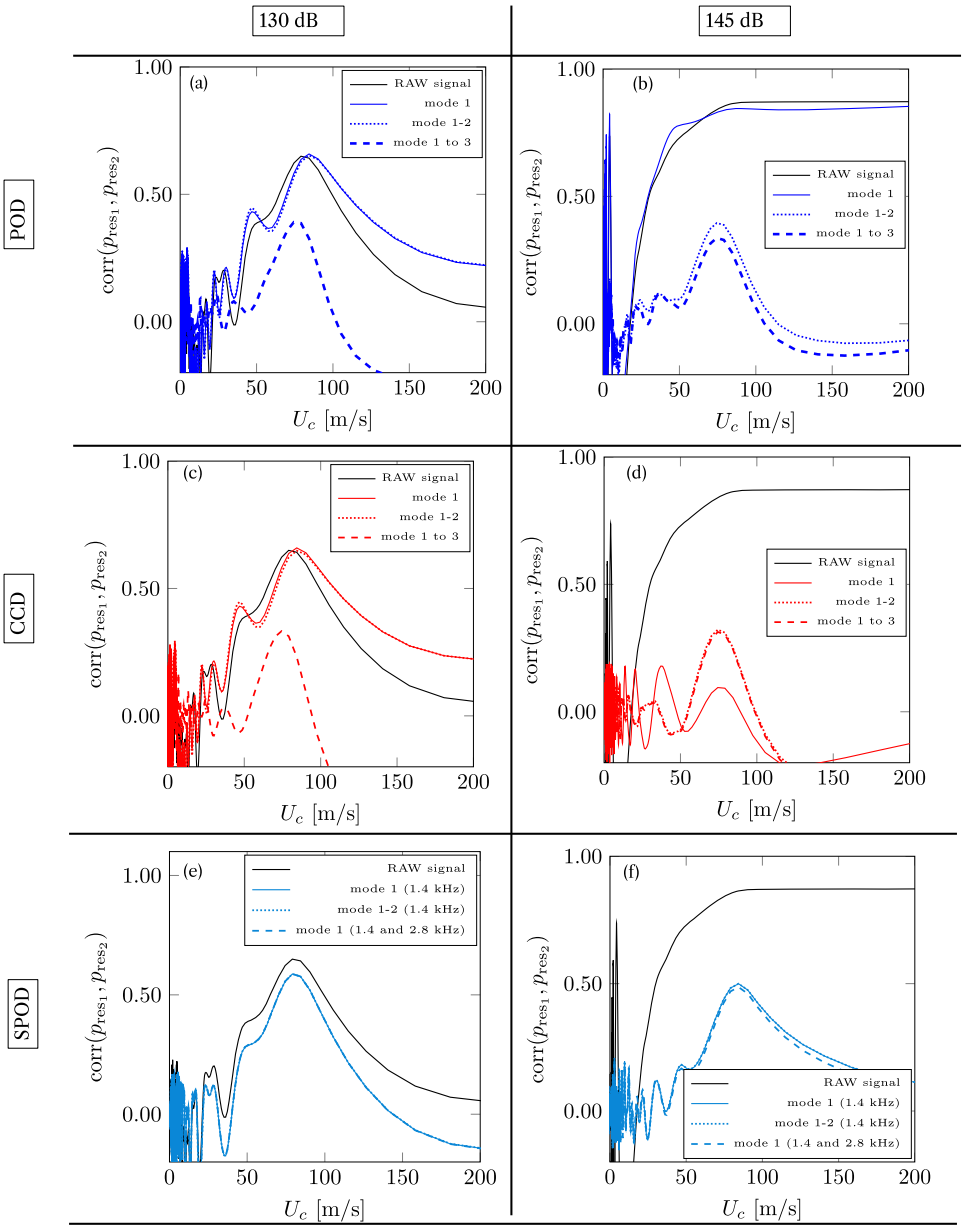

Fig. 16. Normalised cross-correlation of the residual pressure field between the points P1 and P2 depicted in Fig. 1 as a function of convection velocity; left column 130 dB and right columns 145 dB, comparison of the decomposition methods (a-b) POD, (c-d) CCD and (e-f) SPOD.

for the SPOD is illustrated. The cross-correlation of the residual fields and the one computed using the raw pressure signals are reported.

At 130 dB a peak in the raw signals' cross-correlation can be identified, while at 145 dB a peak cannot be discerned. This is because at 130 dB the acoustic fluctuations have an amplitude of the same order of magnitude as the turbulent fluctuations, while at 145 dB the high amplitude acoustic fluctuations overcome the turbulent fluctuations, and if they are not filtered out a correct estimation of the convective velocity cannot be evaluated. The value of the convection velocity found at 130 dB is approximately equal to 79 m/s. This value is close to the mean streamwise velocity at that specific wall-normal location.

Focusing on the results obtained from the residual fields, for the case at 130 dB, the cross-correlation obtained with both POD and CCD appears very similar. Reconstructing the acoustic pressure using the first and second modes gives the same cross-correlation shape, with the cross-correlation peak value similar to the one obtained with the raw signals. However, the peak is shifted towards a larger value of convection velocity; this might be attributed to the effect of the self-tone at 14 kHz that dominates the first two modes at low SPL (see Figs. 16(b) and (e) or 7(a) and (b)). When the third mode is included in the ROM, the amplitude of the

cross-correlation peak decreases because more turbulent velocity fluctuations are filtered. However, the evaluation of the convection velocity approaches the one obtained using the raw signals. The SPOD instead provides always a value of the convection velocity similar to the one obtained from the raw signals.

When increasing the SPL to 145 dB, one can easily note that at least two POD modes must be used in the ROM to obtain a value of the convection velocity similar to the mean streamwise velocity. This is because a non-negligible contribution to the acoustic-induced fluctuations at 1.4 kHz is associated with the second mode, as depicted in the spectra of the coefficients in Fig. 4(c). The CCD results present a discernible peak even considering the residuals obtained by subtracting the reconstructed pressure using the first mode only. However, increasing the number of modes used in the ROM further increases the value of the correlation. The SPOD results are less affected by the number of modes or the different frequency bands, showing a discernible peak with a correlation slightly smaller than 0.5.

A final observation is that, increasing the amplitude of the acoustic wave to 145 dB, the cross-correlation peak of the residual signals has a lower amplitude for all the decompositions than for the 130 dB case. In addition, as shown for SPOD results, the width of the cross-correlation peak is wider when increasing the SPL (Fig. 16(e) and (f)). This might be attributed to a stronger effect of the acoustic waves on the hydrodynamic fluctuations at higher SPL. This means that the acoustic waves modulate the aerodynamic fluctuations at the forcing frequency, and, when subtracting the acoustic-induced reconstructed field, part of the hydrodynamic information is lost.

6. Summary and concluding remarks

Three different modal decomposition methods, POD, CCD, and SPOD, plus the triple decomposition have been tested to separate a fluctuating field (pressure and velocity) into an aerodynamic and an acoustic-induced field. The decompositions are applied to a numerical database representing an orifice of an acoustic liner subjected to grazing flow and acoustic forcing.

A first conclusion is that the performance of the decomposition is strongly influenced by the AHFR, i.e. the relative magnitude of the acoustic-induced field compared to the aerodynamic fluctuations due to turbulence. At high SPL (large AHFR), all decomposition methods produce similar results, whereas at low SPL (low AHFR) significant differences emerge. Therefore, the AHFR represents a key parameter when assessing the reliability of any of the tested methods. A second key parameter that influences the performance is the presence of high-energy and frequency localized disturbances.

The *triple decomposition* method is included in this study because it is widely used in the acoustic liner community [5,6,26]. However, its limitations are severe: the method can only provide one averaged acoustic cycle, without reconstructing a full time series, and it gives no information about the distribution of energy across frequencies. In addition, its reliability quickly deteriorates in the presence of broadband turbulence or localized disturbances (e.g. high-frequency peaks). For these reasons, triple decomposition should mainly be regarded as a reference for comparison with more advanced methods, rather than as a practical tool for analyzing acoustic–turbulence interactions.

POD orders modes by energetic content, which makes it highly sensitive to disturbances that are more energetic than the acoustic forcing. When the acoustic forcing is higher than the amplitude of turbulence, POD provides satisfactory results. However, if other energetic features are present at different frequencies, the acoustic component is no longer captured within the leading modes, and selecting it requires subjective inspection of the mode shapes. This makes the identification less robust and less consistent. An advantage of POD is that it can also be applied to non-time-resolved experimental data, provided the AHFR is sufficiently high. For time-resolved data, POD can capture non-linear effects in higher-order modes, but the interpretation becomes less straightforward. Overall, POD should be used with caution for low AHFR or noisy data.

SPOD highlights energetically relevant features and their distribution across frequencies, making it particularly well suited to problems where the dynamics at the forcing frequency (or frequency band) wants to be investigated. It treats the system linearly, which allows the decomposition of the acoustic-induced velocity into contributions at different frequencies, while non-linear effects appear as separate peaks in the spectrum. A fundamental limitation is that, in turbulent conditions, SPOD cannot completely separate hydrodynamic and acoustic contributions at the same frequency: both appear in the reconstructed field. SPOD requires time-resolved datasets with sufficient sampling frequency and dataset length to enable Fourier transforms and spectral averaging. Its performance depends on parameters such as block size, block overlap, and number of samples, which control the frequency and modal resolution [23]. The sensitivity study reported in the Appendix A shows that, once the window size is large enough to resolve the forcing tone, the reconstructed velocity profiles converge and become insensitive to further parameter changes. This indicates that SPOD is robust when sufficient data are available, although it is not applicable to non-time-resolved datasets.

CCD correlates the flow field with a reference signal, which allows the acoustic-induced field to be isolated without imposing a frequency band a priori. This is advantageous compared to SPOD and triple decomposition, where the acoustic frequency must be specified in advance or identified from the spectrum. Moreover, CCD can capture non-linear effects automatically, as higher harmonics appear naturally in the decomposition. On the other hand, CCD requires a reference signal of sufficient quality. The choice of the reference location is somewhat arbitrary and may affect the results, and if the reference is contaminated by noise the decomposition is strongly degraded. A further advantage of CCD lies in the requirements on the sampling frequencies of the flow field and the observable. The two do not need to be identical: the observable must be sampled at a sufficiently high rate to resolve the frequencies of interest in the flow field, provided that enough snapshots are collected for the correlation matrix to converge. This flexibility can be particularly useful in experimental campaigns where acquisition constraints differ between sensors. CCD is therefore best suited for situations where a reliable reference signal is available (e.g. from a microphone) and the objective is to reconstruct the acoustic-induced velocity (e.g. measured with time-resolved PIV) linked to that source as in the current investigation.

Table 2
Summary of advantages, limitations, and suggested applications of the decomposition methods.

Method	Pros	Cons / Limitations	Suggested applications
Triple dec.	• Straightforward if forcing frequency is known • Provides a basic reference case	• Forcing frequency must be known *a priori* • Poor performance at low AHFR or with frequency-localized disturbances • Only provides a phase-averaged cycle, not a time series • Requires long datasets for convergence • Inefficient at isolating non-linearities • No spectral energy information	• Situations with dominant tonal forcing (visible even in raw data)
POD	• Simple, widely used in the turbulence community • Acoustic field does not need to be known, can work on velocity measurements alone • Applicable to non-time-resolved data • Captures dominant structures at high AHFR • Modes ranked by energy, easy to interpret • No need to know the frequency *a priori* • No arbitrary parameters except for the number of modes for the ROM	• Acoustic mode may not appear among leading modes • Performs poorly at low AHFR, with noisy data, or with strong frequency-localized disturbances • Non-linearities cannot be isolated • Requires subjective inspection of mode shapes	• Useful for first screening of dominant flow features • Suitable for non-time-resolved experimental datasets
CCD	• Efficiently isolates modes correlated with a signal • No arbitrary parameters except for the number of modes for the ROM • Captures non-linear interactions (in higher modes) • Exhibits better low-rank behaviour than POD • The sampling frequency of the observable can be chosen independently of the sampling frequency of the field to be decomposed.	• Requires a clean observable signal • Position of the observable may alter results • Acquisition frequency of the observable must resolve the dynamics of interest	• Ideal for extracting coherent structures correlated with a reference signal (structures either induced by or generating the signal) • Non-linear regimes when the acoustic source signal is known, imposed, or sampled accurately (numerical data) • Well suited for synchronised and time-resolved pressure and velocity experimental measurements
SPOD	• Provides frequency-resolved modal content • Robust at high AHFR • Allows filtering of frequency-localized disturbances • Reconstructs frequency bands of interest • Acoustic field does not need to be known, can work on velocity measurements alone	• Requires long, time-resolved datasets • Forcing frequency must be known or clearly identifiable in spectra (high AHFR) • Hydrodynamic content at reconstruction frequency bands remains in the reconstructed field • Sensitive to window size, overlap, and block number	• Ideal for time-resolved velocity or pressure data (experimental or numerical) without an observable signal • Situations where frequency-resolved modal content is needed

The main characteristics and possible applications of each decomposition method are summarized in Table 2. Ongoing work is focused on combining Helmholtz decomposition with SPOD to quantify the fraction of the coherent acoustic-induced velocity that can also be identified as irrotational.

CRediT authorship contribution statement

Francesco Scarano: Writing – review & editing, Writing – original draft, Visualization, Validation, Software, Methodology, Investigation, Formal analysis, Data curation, Conceptualization; **Benshuai Lyu:** Writing – original draft, Visualization, Methodology, Investigation, Formal analysis, Data curation; **Angelo Paduano:** Writing – original draft, Software, Conceptualization; **Francesco Avallone:** Writing – review & editing, Supervision, Resources, Project administration, Methodology, Investigation, Funding acquisition, Conceptualization.

Ethical Approval: not applicable

Funding: The work of F. Scarano, A. Paduano and F. Avallone is funded by the European Union (ERC, LINING, 101075903). Views and opinions expressed are however those of the author(s) only and do not necessarily reflect those of the European Union or the European Research Council. Neither the European Union nor the granting authority can be held responsible for them.

Availability of data and materials: Data openly available

Data availability

Data will be made available on request.

Declaration of competing interest

The authors declare that they have no known competing financial interests or personal relationships that could have appeared to influence the work reported in this paper.

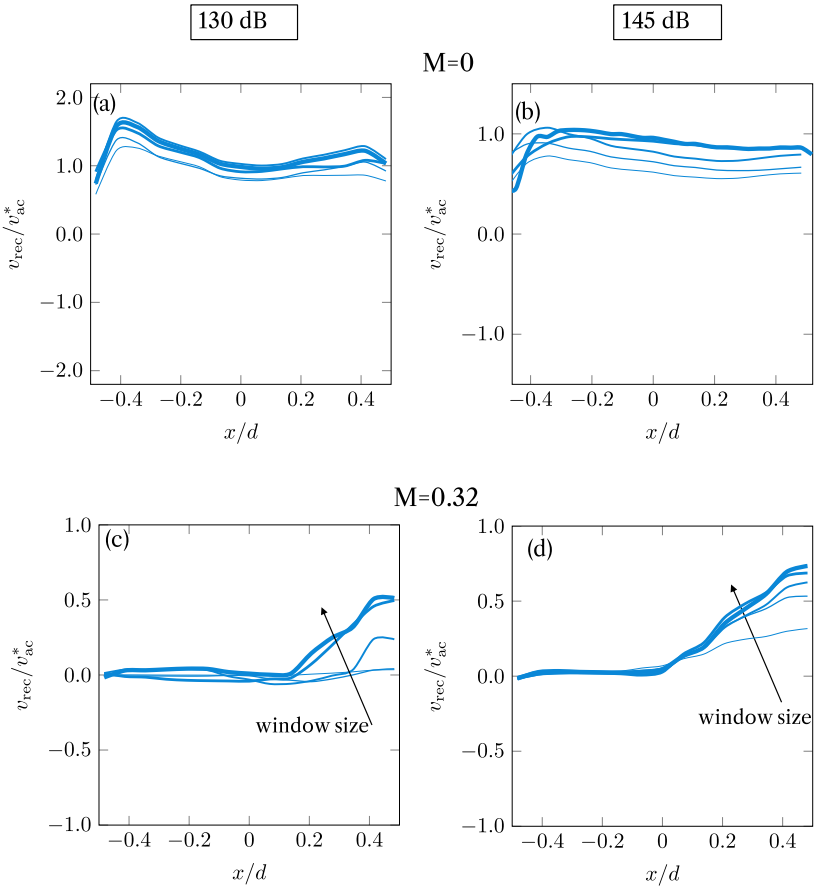

Fig. A.1. Acoustic-induced velocity profiles reconstructed with SPOD for different window sizes 2^m ($m = 7$–11). Thicker lines indicate the tested window sizes. Results are shown for the first SPOD mode, integrated over the frequency bands centered at 1.4 and 2.8 kHz, with a fixed block overlap of 50 %. Increasing the window size improves frequency resolution, and beyond a certain threshold the profiles converge, indicating sufficient resolution to capture the tonal forcing.

Appendix A. Sensitivity of SPOD reconstructions to window size

To assess the robustness of the SPOD reconstruction, we performed a sensitivity analysis on the effect of the window size. Fig. A.1 reports the acoustic-induced velocity profiles obtained for window sizes of 2^m snapshots ($m = 7$–11), with a fixed overlap of 50 %. The results show that small window sizes reduce the frequency resolution, leading to less accurate reconstructions of the velocity profiles. As the window size increases, the reconstructions progressively converge, indicating that the forcing tone is adequately resolved. This effect is analogous to increasing the total number of samples in the dataset.

An additional observation is that the AHFR influences the required window size: in cases with grazing flow at 130 dB, small windows fail to capture the vertical velocity satisfactorily, while larger windows lead to convergence.

Appendix B. Choice of CCD parameters Q and τ_1

The selection of the parameters Q and τ_1 is based on the temporal correlation between the flow and the observable. The correlation matrix $\boldsymbol{A}$ represents a discretized form of the cross-correlation $\overline{p(t+\tau_i)\,u(t,\boldsymbol{x})}$ between the observable and the flow. Each τ_i ($i = 1, 2, \ldots, Q$) corresponds to a distinct time shift, and the total span $(Q-1)\Delta\tau$, with $\Delta\tau = \tau_i - \tau_{i-1}$, defines the effective temporal window of the correlation.

In practice, Q is chosen so that $(Q-1)\Delta\tau$ exceeds the correlation time scale between the observable and the flow. In the present study, Q was set to at least one quarter of the total sampling duration to ensure all relevant correlations are captured. The parameter τ_1 represents the expected time delay between the observable and the flow response. Since the observable is located upstream of the computational domain, τ_1 is expected to be negative, reflecting that the flow response follows the forcing. To ensure robustness, we set τ_1 to a sufficiently large value, $2Q/3f_s$, to cover the full correlation range.

Sensitivity tests were performed by varying Q and τ_1, showing only minor differences in the mode shapes. These results are reported in Fig. B.1, where the line plots of the first and second modes at the orifice centre-line are presented.

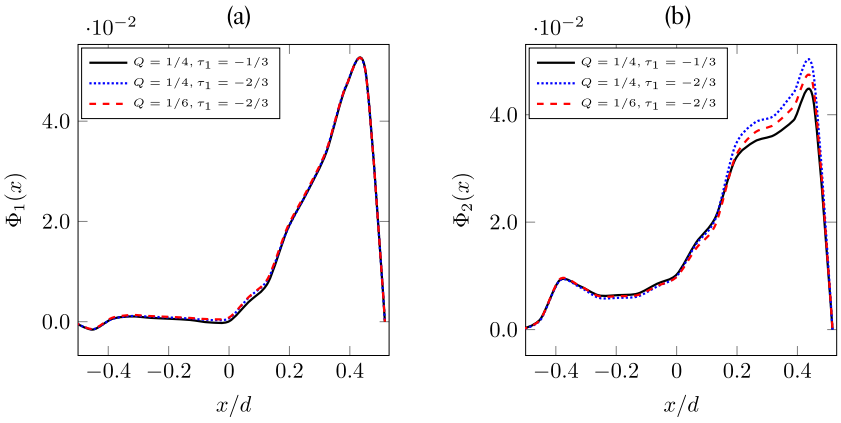

Fig. B.1. CCD normalized modes shapes at the orifice centre-line, effect of changing Q and τ_1 for (a) mode 1, (b) mode 2.

References

[1] M. Mancinelli, T. Pagliaroli, A. Di Marco, R. Camussi, T. Castelain, et al., Wavelet decomposition of hydrodynamic and acoustic pressures in the near field of the jet, J. Fluid Mech. 813 (2017) 716–749. https://doi.org/10.1017/jfm.2016.869

[2] S. Schoder, K. Roppert, M. Kaltenbacher, et al., Postprocessing of direct aeroacoustic simulations using Helmholtz decomposition, AIAA J. 58 (7) (2020) 3019–3027. https://doi.org/10.2514/1.J058836

[3] R.E.A. Arndt, D.F. Long, M.N. Glauser, The proper orthogonal decomposition of pressure fluctuations surrounding a turbulent jet, J. Fluid Mech. 340 (1997) 1–33. https://doi.org/10.1017/S0022112097005089

[4] J.E.F. Williams, Hydrodynamic noise, Annu. Rev. Fluid Mech. 1 (Volume 1, 1969) (1969) 197–222. https://doi.org/10.1146/annurev.fl.01.010169.001213

[5] F. Avallone, D. Casalino, Acoustic-induced velocity in a multi-orifice acoustic liner grazed by a turbulent boundary layer, in: AIAA Aviation and Aeronautics Forum and Exposition, AIAA AVIATION Forum 2021, American Institute of Aeronautics and Astronautics Inc, AIAA, 2021. https://doi.org/10.2514/6.2021-2169

[6] Q. Zhang, D.J. Bodony, Numerical investigation of a honeycomb liner grazed by laminar and turbulent boundary layers, J. Fluid Mech. 792 (2016) 936–980. https://doi.org/10.1017/jfm.2016.79

[7] R. Roncen, F. Méry, E. Piot, F. Simon, Statistical inference method for liner impedance eduction with a shear grazing flow, AIAA J. 57 (3) (2019) 1055–1065. https://doi.org/10.2514/1.J057559

[8] M.S. Howe, The dissipation of sound at an edge, J. Sound Vibr. 70 (3) (1980) 407–411. https://doi.org/10.1016/0022-460X(80)90308-9

[9] R. Tabata, R. Matsuda, T. Koiwaya, S. Iwagami, H. Midorikawa, T. Kobayashi, K. Takahashi, et al., Three-dimensional numerical analysis of acoustic energy absorption and generation in an air-jet instrument based on Howe's energy corollary, J. Acoust. Soc. Am. 149 (6) (2021) 4000–4012. https://doi.org/10.1121/10.0005133

[10] S. Yoshikawa, H. Tashiro, Y. Sakamoto, et al., Experimental examination of vortex-sound generation in an organ pipe: a proposal of jet vortex-layer formation model, J. Sound Vibr. 331 (11) (2012) 2558–2577. https://doi.org/10.1016/j.jsv.2012.01.026

[11] B. Arguillat, D. Ricot, C. Bailly, G. Robert, Measured wavenumber: frequency spectrum associated with acoustic and aerodynamic wall pressure fluctuations, J. Acoust. Soc. Am. 128 (4) (2010) 1647–1655. https://doi.org/10.1121/1.3478780

[12] S. Unnikrishnan, D.V. Gaitonde, A pressure decomposition framework for aeroacoustic analysis of turbulent jets, Eur. J. Mech. B Fluids 81 (2020) 41–61. https://doi.org/10.1016/j.euromechflu.2020.01.006

[13] M. Mancinelli, T. Pagliaroli, R. Camussi, T. Castelain, et al., On the hydrodynamic and acoustic nature of pressure proper orthogonal decomposition modes in the near field of a compressible jet, J. Fluid Mech. 836 (2018) 998–1008. https://doi.org/10.1017/jfm.2017.839

[14] P.J. Schmid, Dynamic mode decomposition of numerical and experimental data, J. Fluid Mech. 656 (2010) 5–28. https://doi.org/10.1017/S0022112010001217

[15] H. Vincent, C. Bogey, Influence of the boundary-layer thickness on the generation of tonal noise components by subsonic impinging jets, J. Fluid Mech. 985 (2024) A26. https://doi.org/10.1017/jfm.2024.281

[16] R. Ewert, W. Schröder, Acoustic perturbation equations based on flow decomposition via source filtering, J. Comput. Phys. 188 (2) (2003) 365–398. https://doi.org/10.1016/S0021-9991(03)00168-2

[17] S. Schoder, E. Spieser, H. Vincent, C. Bogey, C. Bailly, Acoustic modeling using the aeroacoustic wave equation based on Pierce's operator, AIAA J. 61 (9) (2023) 4008–4017. https://doi.org/10.2514/1.J062558

[18] S. Grizzi, R. Camussi, Wavelet analysis of near-field pressure fluctuations generated by a subsonic jet, J. Fluid Mech. 698 (2012) 93–124. https://doi.org/10.1017/jfm.2012.64

[19] T. Brunner, T. Kroissenbrunner, A. Wurzinger, S. Schoder, Acoustic resonances and aeroacoustic feedback mechanisms occurring at a deep cavity with an overhanging lip, J. Sound Vibr. 606 (2025) 119004. https://doi.org/10.1016/j.jsv.2025.119004

[20] G. Berkooz, P. Holmes, J.L. Lumley, The proper orthogonal decomposition in the analysis of turbulent flows, Annu. Rev. Fluid Mech. 25 (Volume 25, 1993) (1993) 539–575. https://doi.org/10.1146/annurev.fl.25.010193.002543

[21] J. Weiss, A tutorial on the proper orthogonal decomposition, in: AIAA Aviation 2019 Forum, American Institute of Aeronautics and Astronautics, Dallas, Texas, 2019. https://doi.org/10.2514/6.2019-3333

[22] A. Towne, O.T. Schmidt, T. Colonius, et al., Spectral proper orthogonal decomposition and its relationship to dynamic mode decomposition and resolvent analysis, J. Fluid Mech. 847 (2018) 821–867. https://doi.org/10.1017/jfm.2018.283

[23] O.T. Schmidt, T. Colonius, Guide to spectral proper orthogonal decomposition, AIAA J. 58 (3) (2020) 1023–1033. https://doi.org/10.2514/1.J058809

[24] B. Lyu, Canonical correlation decomposition of numerical and experimental data for observable diagnosis, in: 30th AIAA/CEAS Aeroacoustics Conference, 2024, pp. AIAA 2024–3206.

[25] B. Lyu, Canonical correlation decomposition of numerical and experimental data for observable diagnosis, (2025). arXiv preprint v2, arXiv:2312.14858

[26] O. Léon, F. Méry, E. Piot, C. Conte, Near-wall aerodynamic response of an acoustic liner to harmonic excitation with grazing flow, Exp. Fluids 60 (9) (2019). https://doi.org/10.1007/s00348-019-2791-5

[27] J.L. Lumley, The structure of inhomogeneous turbulent flows, Atmos. Turbul. Radio Wave Propag. (1967) 166–177.

[28] A. Paduano, L.M. Pereira, L.A. Bonomo, J.A. Cordioli, D. Casalino, F. Avallone, On the impact of the acoustic wave direction on the in-orifice flow dynamics of an acoustic liner grazed by a turbulent flow, in: 30th AIAA/CEAS Aeroacoustics Conference, 2024.

[29] X. He, L.S. Luo, Theory of the lattice Boltzmann method: from the Boltzmann equation to the lattice Boltzmann equation, Phys. Rev. E Stat. Phys. Plasmas Fluids Relat. Interdiscip. Top. 55 (6) (1997). https://doi.org/10.1103/PhysRevE.56.6811

[30] P.L. Bhatnagar, E.P. Gross, M. Krook, A model for collision processes in gases. i. small amplitude processes in charged and neutral one-component systems, Phys. Rev. 94 (3) (1954). https://doi.org/10.1103/PhysRev.94.511
[31] Y.H. Qian, D. D'Humières, P. Lallemand, Lattice BGK models for Navier-Stokes equation, EPL 17 (6) (1992). https://doi.org/10.1209/0295-5075/17/6/001
[32] V. Yakhot, S.A. Orszag, Renormalization-group analysis of turbulence, Phys. Rev. Lett. 57 (14) (1986). https://doi.org/10.1103/PhysRevLett.57.1722
[33] L.A. Bonomo, A.M.N. Spillere, J.A. Cordioli, Parametric uncertainty analysis for impedance eduction based on prony's method, AIAA J. 58 (8) (2020). https://doi.org/10.2514/1.J059071
[34] A. Paduano, F. Scarano, J. Cordioli, D. Casalino, F. Avallone, On the impact of the turbulent grazing flow development on the acoustic response of an acoustic liner, (2025). arXiv preprint arXiv:2507.22714
[35] C.K.W. Tam, H. Ju, M.G. Jones, W.R. Watson, T.L. Parrott, et al., A computational and experimental study of resonators in three dimensions, J. Sound Vibr. 329 (24) (2010) 5164–5193. https://doi.org/10.1016/j.jsv.2010.06.005
[36] C.K.W. Tam, K.A. Kurbatskii, Microfluid dynamics and acoustics of resonant liners, AIAA J. 38 (8) (2000) 1331–1339. https://doi.org/10.2514/2.1132
[37] F. Scarano, A. Paduano, F. Avallone, Acoustic liners' dissipation analysis in presence of grazing flow using Howe's energy corollary, in: 54th International Congress and Exposition on Noise Control Engineering, InterNoise 2025, 2025.
[38] R.L. Panton, J.M. Miller, Resonant frequencies of cylindrical Helmholtz resonators, J. Acoust. Soc. Am. 57 (6) (1975) 1533–1535. https://doi.org/10.1121/1.380596
[39] G. Dacome, R. Siebols, W.J. Baars, Small-scale Helmholtz resonators with grazing turbulent boundary layer flow, J. Turbul. 25 (12) (2024) 461–481. https://doi.org/10.1080/14685248.2024.2412586
[40] P.M.C. Morse, K.U. Ingard, P.M. Morse, Theoretical Acoustics: By Philip M. Morse and K. Uno Ingard, McGraw-Hill, 1968. https://books.google.it/books?id=NmQAyAEACAAJ.
[41] T. Utami, R.F. Blackwelder, T. Ueno, A cross-correlation technique for velocity field extraction from particulate visualization, Exp. Fluids 10 (4) (1991) 213–223. https://doi.org/10.1007/BF00190391